# EXPERIMENTAL AND NUMERICAL INVESTIGATION OF FRETTING FAILURE IN LUG-BUSH MEMBERS UNDER CYCLIC LOADING

A THESIS SUBMITTED TO
THE GRADUATE SCHOOL OF NATURAL AND APPLIED SCIENCES
OF
MIDDLE EAST TECHNICAL UNIVERSITY

BY

EMİNE BURÇİN ÖZEN

IN PARTIAL FULFILLMENT OF THE REQUIREMENTS
FOR
THE DEGREE OF MASTER OF SCIENCE
IN
AEROSPACE ENGINEERING

JULY 2021

Approval of the thesis:

**EXPERIMENTAL AND NUMERICAL INVESTIGATION OF FRETTING FAILURE IN LUG-BUSH MEMBERS UNDER CYCLIC LOADING**

submitted by **EMİNE BURÇİN ÖZEN** in partial fulfillment of the requirements for the degree of **Master of Science** i**n Aerospace Engineering, Middle East Technical University** by,

Prof. Dr. Halil Kalıpçılar
Dean, Graduate School of **Natural and Applied Sciences** _____

Prof. Dr. İsmail H. Tuncer
Head of the Department, **Aerospace Engineering** _____

Prof. Dr. Demirkan Çöker
Supervisor, **Aerospace Engineering, METU** _____

**Examining Committee Members:**

Assoc. Prof. Dr. Ercan Gürses
Aerospace Engineering, METU _____

Prof. Dr. Demirkan Çöker
Aerospace Engineering, METU _____

Assoc. Prof. Dr. Tuncay Yalçınkaya
Aerospace Engineering, METU _____

Prof. Dr. Altan Kayran
Aerospace Engineering, METU _____

Prof. Dr. Erdem Acar
Mechanical Engineering, TOBB University _____

Date: 16.07.2021

**I hereby declare that all information in this document has been obtained and presented in accordance with academic rules and ethical conduct. I also declare that, as required by these rules and conduct, I have fully cited and referenced all material and results that are not original to this work.**

Name, Surname: Emine Burçin Özen

Signature:

# ABSTRACT

## EXPERIMENTAL AND NUMERICAL INVESTIGATION OF FRETTING FAILURE IN LUG-BUSH MEMBERS UNDER CYCLIC LOADING

Özen, Emine Burçin
Master of Science, Aerospace Engineering
Supervisor: Prof. Dr. Demirkan Çöker

July 2021, 86 pages

In this study, experimental and numerical work to investigate the mechanisms occurring at the contact region of the lug-bush members under cyclic loading are presented. Post-mortem macroscopic and microscopic investigations of the mating lug and bush surfaces are conducted using digital microscope and scanning electron microscope. The black-brown residues observed at the mating surfaces are shown to be tribolayer regions using energy dispersive spectroscopy analysis. Locations of sliding regions at the contact surfaces are identified by considering the locations of tribolayer regions which indicate the existence of relative sliding. Crack initiation locations are observed to be in the vicinity of the boundary between the sticking and sliding regions. In order to investigate the mechanisms occurring at the contact surfaces during cyclic loading, a 3-dimensional finite element model is created and cyclic loads are applied. It is observed that the steady state response is reached during the $2^{nd}$ cycle when sliding region areas and relative sliding distances are compared. This result verifies that the application of the cyclic loading is crucial in order to evaluate the behavior using the steady state response. For each material combination, type and sequence of contact mechanisms are observed to be different. A parametric study on the effect of friction coefficient is presented. Increase in the value of friction

coefficient leads to decrease in the size of sliding regions. Fatemi-Socie and Smith-Watson-Topper multiaxial fatigue damage parameters are applied in order to predict the crack initiation locations. It is shown that these parameters are not able to predict the crack locations of the specimens. In fact, boundaries of the sticking-sliding regions obtained from the simulations are able to predict the crack initiation locations. Good correlation is obtained between the sliding regions observed in the experiments and simulations when the experimental disturbances are taken into consideration in the simulations.

Keywords: Fretting fatigue, Sticking-sliding regions, Slip-front velocity, Fatigue damage parameters

# ÖZ

## PABUÇ-BURÇ ELEMANLARINDA ÇEVRİMSEL YÜK ALTINDA MEYDANA GELEN TİTREŞİMLİ AŞINMA HASARININ DENEYSEL VE NÜMERİK OLARAK İNCELENMESİ

Özen, Emine Burçin
Yüksek Lisans, Havacılık ve Uzay Mühendisliği
Tez Yöneticisi: Prof. Dr. Demirkan Çöker

Temmuz 2021, 86 sayfa

Bu çalışmada, pabuç-burç bağlantı parçalarının çevrimsel yük altında temas yüzeylerinde oluşan mekanizmalar deneysel ve nümerik olarak incelenmiştir. Test edilmiş olan pabuç-burç numunelerinin temas alanları kamera, dijital mikroskop ve taramalı electron mikroskobu ile makro ve mikro düzeylerde gözlemlenmiştir. Temas yüzeylerinin Enerji Dağılım Spektrometresi yöntemi ile incelenmesi ile kayma bölgelerinin alanları ve konumları belirlenmiştir. Pabuçlarda oluşan kırılmaların, kayma ve tutunma bölgelerinin sınırlarına yakın bir konumda oluştuğu gözlemlenmiştir. Temas yüzeylerinde çevrimsel yük sırasında oluşan mekanizmaları incelemek için 3 boyutlu bir sonlu elemanlar modeli geliştirilmiştir. Sonlu elemanlar modelinde uygulanan çevrimsel yükün periyodik davranışa dönüşmesi için gereken çevrim sayısı, analiz sonuçları değerlendirilerek belirlenmiştir. Bu değerlendirme sonucunda, yorulma hasar parametrelerinin kullanıldığı durumlarda çevrimsel yük uygulanması ve periyodik davranışın elde edildiği çevrimin sonuçlarının kullanılması gerektiği görülmüştür. Nümerik analizler sonucunda yük-deplasman grafiklerinde gözlemlenen histerez davranışı ve temas yüzeylerinde oluşan farklı temas mekanizmaları detaylandırılmıştır. Farklı sürtünme katsayıları kullanılarak

yapılan parametrik çalışmanın sonuçları sunulmuştur. Sürtünme katsayısı arttıkça kayma alanlarının küçüldüğü gözlemlenmiştir.

Anahtar Kelimeler: Titreşimli aşınma yorulması, Kayma-tutunma bölgeleri, Yorulma hasar parametreleri

*To the memory of my beloved friend, Ozancan Akkuş*

*Rest in peace…*

## ACKNOWLEDGMENTS

My foremost thanks must go to Prof. Demirkan Çöker, who supervised me during my BSc and MSc studies. I am grateful for his peerless guidance and support. I am also grateful to Yezdan Medet Korkmaz for his valuable contributions throughout the evaluation of experimental observations. I would also like to thank Baran Güler and Dr. Mert Efe for their help with the SEM and EDS analyses.

I would like to thank the members of DKTM project, Prof. Kemal Levend Parnas, Burak Ogün Yavuz, and Saeid Dashatan for their wonderful collaboration. I would also like to acknowledge the whole RÜZGEM community and Prof. Oğuz Uzol, head of RÜZGEM, for providing me a peaceful working place and for offering me the opportunity to use RÜZGEM facilities.

I would like to thank Assoc. Prof. Ercan Gürses, Assoc. Prof. Tuncay Yalçınkaya, Prof. Altan Kayran, and Prof. Erdem Acar for attending my thesis defense presentation and contributing to this research with their valuable comments.

I would like to thank the Coker Research Group members during my MSc studies, Ahmet Çevik, Burcu Taşdemir, Tamer Tahir Ata, Aydın Amireghbali, Can Muyan, Tutku Ilgın Özcan, Umut Altuntaş, and Onur Ali Batmaz for their valuable friendship and assistance throughout the study.

I would like to express my deepest gratitude to Miraç Onur Bozkurt for his love, his patience, and his advice. His valuable comments contributed greatly to this study. Last but not least, I would like to thank my family – my father Ahmet Özen, my mother Şükran Özen, my dear sister Betül Ero, and my beloved nephew Rüzgar Mert Ero – for their endless love and support throughout the study. Thank you for your encouragement and never-ending faith in me.

## TABLE OF CONTENTS

## LIST OF TABLES

TABLES

## LIST OF FIGURES

FIGURES

## LIST OF ABBREVIATIONS

ABBREVIATIONS

| | |
|---|---|
| EDS | Energy Dispersive Spectroscopy |
| FEA | Finite Element Analysis |
| FEM | Finite Element Model |
| FS | Fatemi-Socie |
| LHS | Left-hand side |
| RHS | Right-hand side |
| SEM | Scanning Electron Microscope |
| SWT | Smith-Watson-Topper |

## LIST OF SYMBOLS

SYMBOLS

| | |
|---|---|
| $\mu$ | Friction coefficient |
| $\Delta\gamma_{max}$ | Maximum shear strain amplitude |
| $\sigma_{n,max}$ | Maximum normal stress acting on the critical plane |
| $\sigma_y$ | Yield strength |
| $k$ | Material constant for FS parameter |
| $\Delta\varepsilon$ | Normal strain amplitude |
| $R$ | Stress ratio in cyclic loading |
| $L$ | Maximum applied resultant load in a cycle |
| $p$ | Internal pressure acting on the bush |
| $d$ | Inner diameter of the bush |
| $\theta$ | Angular position on the mating surface |
| $\gamma$ | Relative sliding distance (slip) |
| $\gamma_{el}{}^{crit}$ | Critical elastic slip |
| $\gamma_r$ | Residual slip |
| $\tau$ | Contact shear stress |
| $\tau_{crit}$ | Critical contact shear stress |
| *FS* | Fatemi-Socie parameter |
| *SWT* | Smith-Watson-Topper parameter |

# CHAPTER 1

# INTRODUCTION

Fretting is a contact condition which is defined as the minute relative motion between contacting bodies due to oscillations or cyclic loads. These cyclic loads cannot create a bulk motion between contacting bodies; however, create partial regions at the contact area where small-amplitude relative motion is observed. The partial regions which experience relative motion are called *sliding regions*. The remaining regions of the contact area are called *sticking regions* since the contacting bodies do not experience relative motion at these regions. Occurrence of the fretting phenomena at a contact area subject to fatigue loading is called *fretting fatigue*.

Fretting fatigue is observed and reported for the first time in 1911 by Eden et al. [1] at the contact region of specimens and grips during the plain fatigue tests. Fretting fatigue is also observed over a wide range of applications such as hip prostheses, flexible marine risers, wire ropes, railway axles, bolted joints, dovetail blade roots, pin-loaded joints, and shrink-fitted assemblies [2-9]. Studies investigating the fatigue lives of specimens under fretting conditions show that dramatic decreases in fatigue lives are observed if fretting takes place [10,11]. Since many critical industrial applications such as aerospace and nuclear power generations face fretting fatigue failures, there has been interest to study the the mechanisms behind the fretting phenomena for decades both analytically, numerically, and experimentally.

Most of the experimental studies on fretting fatigue investigated the effects of different factors on the fretting fatigue mechanisms. An early study on the influencing factors of fretting fatigue suggests that there are over 50 parameters affecting the fretting mechanism [12]. These experimental studies used a fretting test apparatus consisting of cylindrical pads on a flat specimen [13,14] since the closed

form solutions of the stresses can be obtained in this configuration. A rather small amount of experimental studies investigated the fretting fatigue in specific actual components such as dovetails or bolted joints and focused on the fretting fatigue life of the investigated components [15,16].

Several numerical studies also investigated the fretting fatigue in actual components and the common purpose of these studies was the prediction of the life spent until the initiation of a crack or the prediction of crack locations and comparison with the experimentally obtained fatigue lifes [15,16]. Generally, the details of the mechanisms occurring at the contact area are not included in the scope of these studies. For the calculations of the fatigue life predictions due to crack growth, different multiaxial fatigue damage parameters adopting the critical plane approach are applied to the numerical results of actual components. These multiaxial fatigue damage parameters require the stress and strain values reached during one cycle for the calculation of critical planes. The studies employing these parameters model the first cycle of fatigue loading and use the stress and strain values obtained from that cycle.

The aim of this study is to investigate the fretting mechanisms occurring at the contact region of an actual connection member under cyclic loading which is used widely in the aerospace industry and called a lug-bush member. For this purpose, four tested lug-bush members are observed using both macroscopic and microscopic observation methods and these observations are summarized in Chapter 2. In order to observe the mechanisms and evolution of events occurring at the contact region of the lug-bush members during cyclic loadings, a numerical study is conducted. A 3-D implicit dynamic Finite Element Model (FEM) is created at the testing conditions of the observed lug-bush members. The numerical results obtained from the Finite Element Analyses (FEA) are compared with the post-mortem observations of the tested lug-bush specimens. The maximum sliding regions obtained from the FEA results during cyclic loading are compared with the tribolayer locations observed in the mating bush surfaces of the tested specimens. Another comparison between the FEA results and post-mortem observations are conducted by employing

two multiaxial fatigue damage parameters, namely Fatemi-Socie (FS) and Smith-Watson-Topper (SWT), and predicting the crack initiation locations. Details of the FEM and the multiaxial fatigue damage parameters are described in Chapter 3. In Chapter 4, the results of the FEA describing the sequence and type of events occurring at the contact region are presented with a parametric study on friction coefficient values. Fatemi-Socie and Smith-Watson-Topper damage parameters are evaluated using the results of FEA. Finally, the conclusions of this experimental and numerical study are reported in Chapter 5.

# CHAPTER 2

# EXPERIMENTAL OBSERVATIONS

Four specimens, which are called lug-bush members, were tested under fatigue loading conditions. A lug-bush member consists of a lug with two circular holes at each end and two bushes which are assembled into these holes with interference fit. The experimental program of the specimens, whose post-mortem observations will be discussed in this paper, is conducted at Turkish Aerospace Industries.

## 2.1 Experimental conditions

The details of the four specimens are shown in Figure 2.1. Two lug-bush members, namely Specimens A and B, have the same material combination: a titanium lug and steel bushes. The third specimen, Specimen C, has aluminum lug and steel bushes while the fourth specimen, Specimen D, consists of aluminum lug and aluminum bushes. Specimens A, B, and C have dissimilar materials for their lugs and bushes, whereas Specimen D has the same material. Mechanical properties of these materials are given in Table 2.1.

Table 2.1. Material properties.

| **Material** | **E [GPa]** | **ν** | **ρ [kg/m$^3$]** |
|---|---|---|---|
| Aluminum | 70 | 0.33 | 2820 |
| Titanium | 110 | 0.31 | 4430 |
| Steel | 196 | 0.27 | 7830 |

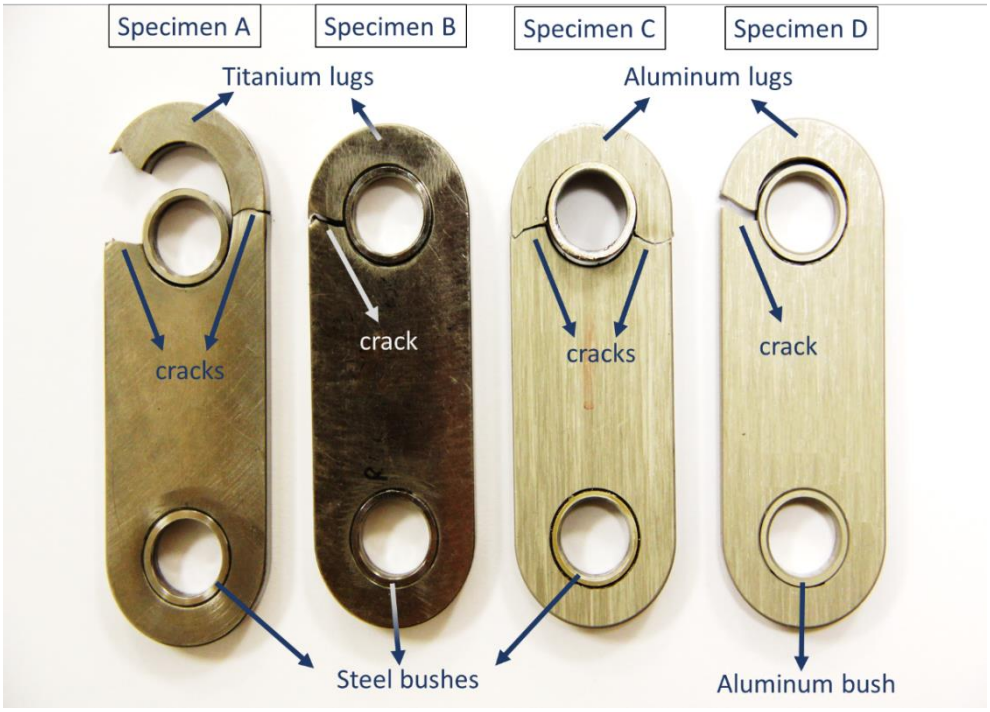


Figure 2.1. Post-mortem pictures of all specimens and the cracks in the lugs.

Fatigue tests of all specimens were conducted using Rumul fatigue testing machine until failure at a frequency of 90 Hz and at a stress ratio of $R = 0.1$. Loading is applied to the specimens with two pins, each passing through the bushes. The maximum applied force values by the pins to the inner surface of the bushes for each specimen are given in Table 2.2. The tests were stopped upon failure of the lug and at the end of each test, the bushes were still intact. Failure of the lug occurred due to a crack initiated at the contact surface of the lug and bush and propagated towards the outer edge of the lug.

Table 2.2. Maximum applied force values by the pins to the specimens during experiments.

| **Specimen** | A | B | C | D |
|---|---|---|---|---|
| **Maximum applied force [kN]** | 19.9 | 19.9 | 7.2 | 4.9 |

## 2.2 Macroscopic observations

Macroscopic observations of the failed lug-bush members are conducted by eye-inspection and using a digital camera. These observations revealed discontinuous black residues on the contacting surfaces of the lugs and bushes. Figure 2.2 shows the residues on the mating lug and bush surfaces of Specimen A. The residues on the lug inner surfaces and bush outer surfaces are observed to be matching for each specimen. Using these matching residues, the corresponding crack initiation locations of the lug are identified on the bush surfaces. Further macroscopic observations on the contacting lug surfaces shows that the black residues exist at only one side of the crack, as seen in Figure 2.2 for Specimen A.

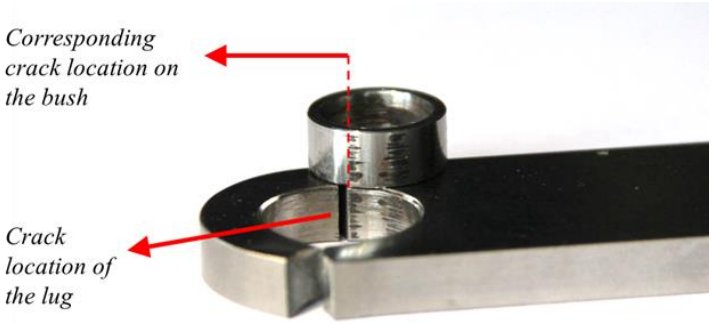


Figure 2.2. Crack location of the lug and the corresponding crack location on the bush mating surface.

The existence of black residues is assumed to be linked to the relative displacements occurring between the contacting surfaces, as observed experimentally in many studies. Therefore, the regions with black residues on both the lug and bush mating surfaces are assumed to experience relative sliding under fatigue loading which are called *sliding regions*. Whereas the clean regions on mating surfaces which are free from any residue are assumed to stick together by experiencing no relative motion and these regions are called *sticking regions*. Also, the reason behind the black-brown color of the residues is predicted as the oxidation of the wear particles produced by the relative sliding motions.

Locations of the sticking and sliding regions of all specimens are mapped as shown in Figure 2.3 by identifying the locations of the black residues on the bush mating surfaces. The red lines in the maps represent the sliding regions. Remaining surfaces were free from any residues and are represented with blue, indicating the sticking surfaces. The corresponding crack locations on the bush mating surfaces are also identified on the map. These cracks were found to initiate near the boundary of sticking and sliding regions after which it propagated, breaking one side of the lug. The location of the boundaries between the sticking and sliding regions lie at 100° - 105°, as shown in Figure 2.3. The reason for the difference in sliding region representation of Specimen D is the rounded tribolayer shape, unlike the directional shape observed in the first three specimens.

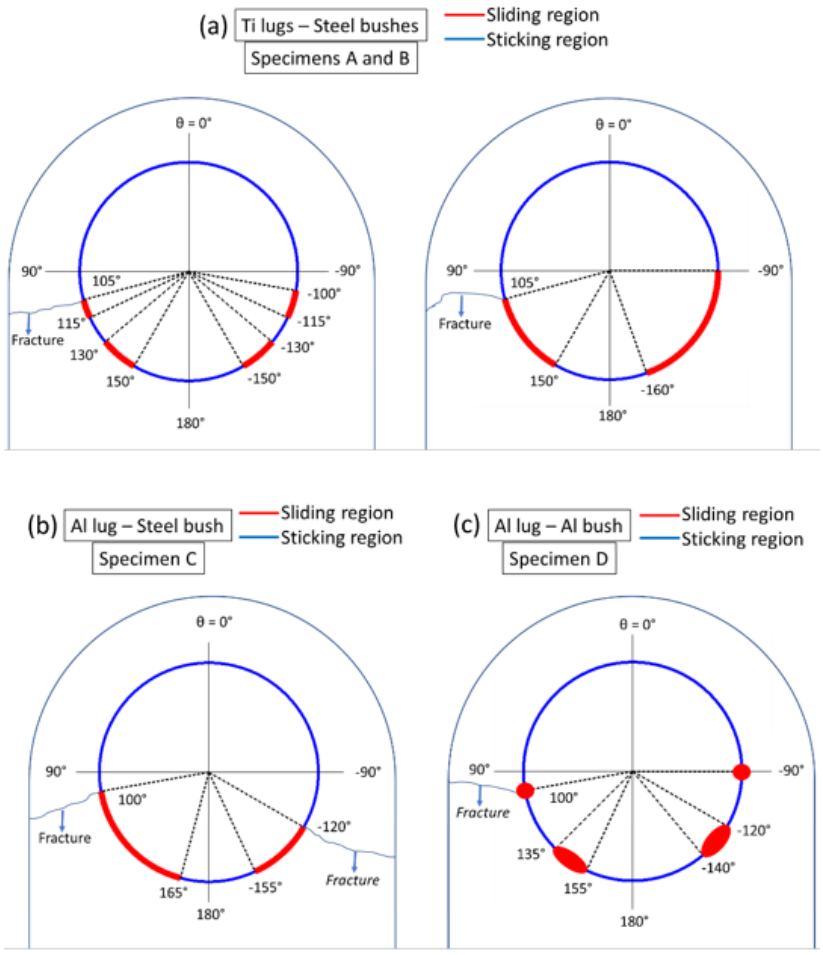


Figure 2.3. Experimental sticking and sliding region maps of all specimens.

## 2.3 Microscopic observations

In order to clarify the abovementioned predictions about the fretting fatigue mechanisms occurring at the contact regions, microscopic observations are conducted using a digital microscope (Huvitz HDS-5800) and a Scanning Electron Microscope (SEM) on the bush mating surface of Specimen A. The lug mating surface of Specimen A is not observed microscopically due to its shape and also the size limitations of the specimen chamber of SEM.

The corresponding crack location on the bush mating surface of Specimen A is observed under digital microscope at 200x magnification, as shown in Figure 2.4(a). In the micrograph, the sharp boundary between the sticking and sliding regions can be observed easily. This boundary continues throughout the whole thickness direction and corresponds to the vicinity of the crack location of the lug, as observed in the macroscopic observations shown in Figure 2.2. Figure 2.4(b) shows the scanning electron micrograph of the bush mating surface of Specimen A under 1300x magnification. Both the black residues and the clean regions, in other words the sliding and sticking regions (clean surface at the left bottom of the scanning electron micrograph), respectively, can be seen in Figure 2.4(b).

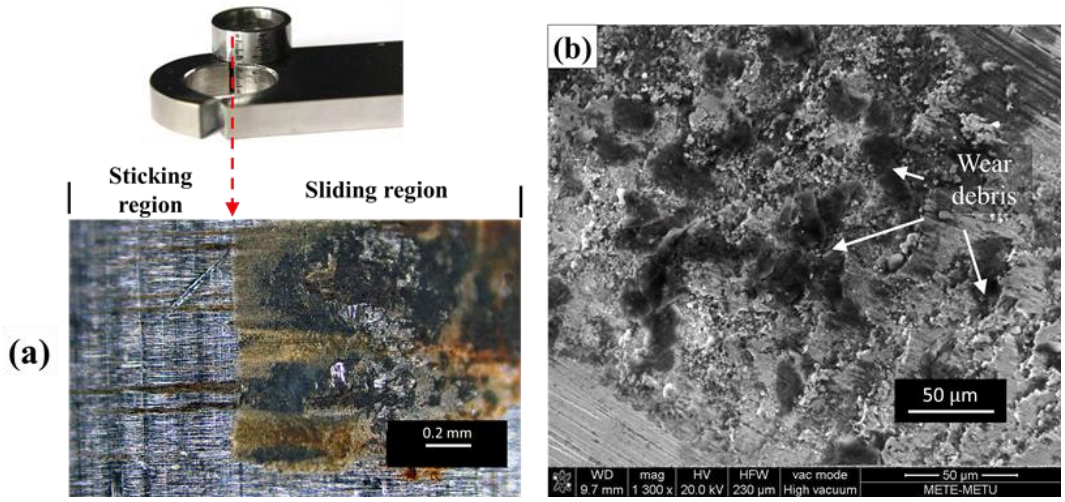


Figure 2.4. (a) Micrograph of the boundary between sticking and sliding regions of Specimen A and (b) scanning electron micrograph of the sliding region of Specimen A under 1300x magnification.

Further microscopic investigations are conducted through Energy Dispersive Spectroscopy (EDS) analysis using the SEM. This method is used for the determination of elemental composition of the sticking and sliding regions in order to identify the reasons for the difference in the colors of these regions. The EDS spectrums obtained from the sticking and sliding regions are summarized in Table 2.3. The analysis shows that the sliding region contains significant amount of oxygen (20% by mass) unlike the sticking regions where no oxygen content is detected. In the sliding regions, the fine metallic particles worn from the mating surfaces are oxidized and attained a black-brown color that are observed in the micrographs. This resultant product of oxidized fine metallic particles is called tribolayer [20]. The frictional behaviors of the two mating surfaces are determined by the characteristics of the tribolayer formed [21].

Table 2.3. EDS spectrums of the sticking and sliding regions of bush mating surface of Specimen A.

| | **Sliding Region** | **Sticking Region** |
|---|---|---|
| **Elemental Composition [wt%]** | 63.36% Ti | 76.94% Fe |
| | 20.45% O | 15.39% Cr |
| | 11.45% C | 4.02% Ni |
| | 4.74% Al | 3.65% Cu |

Sticking-sliding regions of the four different lug-bush members are compared. The shape of tribolayer regions of specimens A, B, and C, which have dissimilar lug and bush materials, are observed to be directional and discontinuous as shown in Figure 2.5(a). However, in Al-Al lug-bush specimen (specimen D) the tribolayer regions have rounded shapes in contrary to other three specimens, as shown in Figure 2.5(b). Considering this difference between tribolayer shapes, the sliding regions of Al-Al lug-bush specimen (Specimen D) are shown with rounded red shapes on the sticking and sliding region map (Figure 2.3).

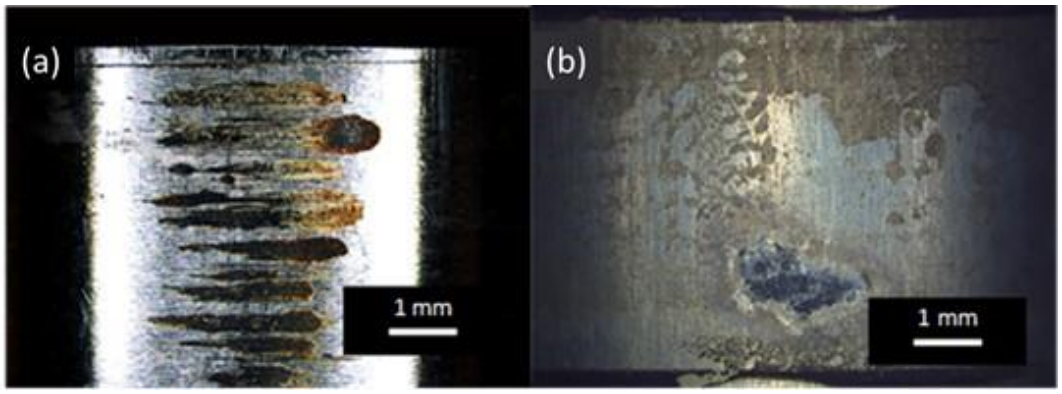


Figure 2.5. The tribolayer shapes observed on the bush surfaces of (a) Ti-steel lug-bush specimen (specimen A) and (b) Al-Al lug-bush specimen (specimen D), at 50x magnification.

# CHAPTER 3

# NUMERICAL METHOD

In this chapter, finite element model of the lug-bush member under cyclic loading, the contact algorithm implemented in this problem, and definitions of the fatigue damage parameters used to predict the fretting crack location on the lug members are presented.

## 3.1 Finite element model

In order to simulate the experimental fatigue loading conditions of lug-bush connection members, a three-dimensional finite element model is created in ABAQUS/Standard. Due to the symmetry of the loading and the specimen in xz-plane, half of the lug-bush member is modeled using the dimensions of the tested specimens, as shown in Figure 3.1(a). Both the lug and the bush are discretized with 20-noded 3-D quadratic solid elements (C3D20), as shown in Figure 3.1(b). The mesh is refined around the contact area of the lug, having a distance of approximately 0.1 μm between adjacent nodes. At the bottom surface of the lug, symmetry condition in y-direction is defined as shown in Figure 3.1(c), restricting the displacement in y-direction and the rotations around x- and z-axes. The node resting at the middle of this symmetry surface is fixed in all directions. The materials used are defined as elastically isotropic and their properties are summarized in Table 2.1. A static friction coefficient is defined for the contact between the lug and the bush.

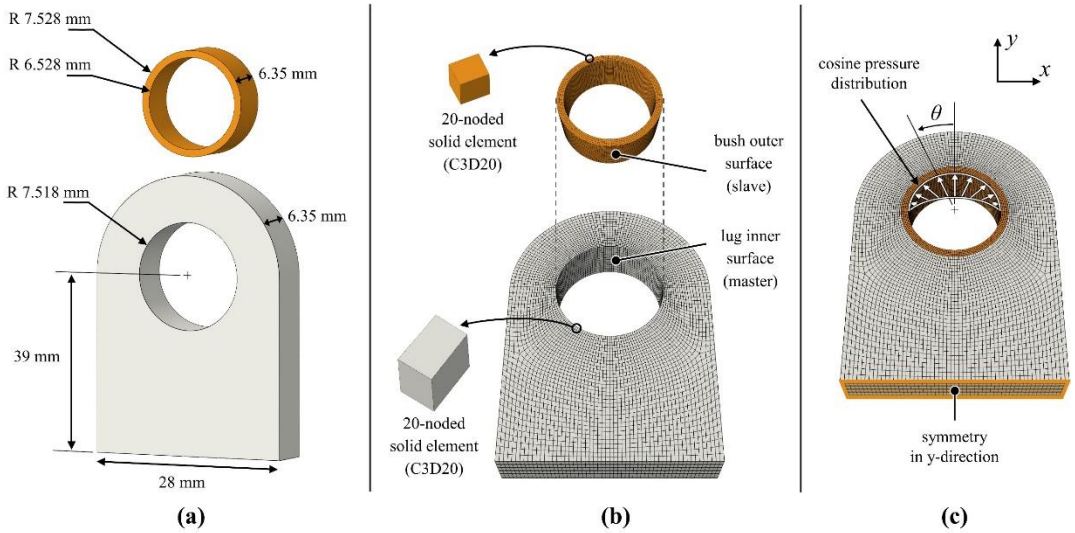


Figure 3.1. Details of the FEM showing (a) dimensions, (b) element types and master-slave surfaces, and (c) loading and symmetry boundary condition.

The solution is performed in two steps. In the first step of the solution, interference fit of the bush inside the lug is defined. An initial penetration of 0.01 mm between the lug and the bush is resolved linearly during this step by gradual removal of slave node overclosures. In the second step, the analysis method is changed from static implicit to dynamic implicit. In this step, a cyclic pressure is applied to the inner upper half surface of the bush in cosine form, as shown in Figure 3.1(c), in order to represent a loading applied by a pin [17,18]. Figure 3.2 shows the amplitude of normalized applied pressure with respect to time of the 2nd step of the solution. The loading includes four cycles with stress ratio of $R$ = 0.1 and the duration of each cycle is selected as 11100 μs so that the loading frequency is equal to 90 Hz as in the experiments. The loading is applied in four cycles due to repeatability concerns. A study which is performed to obtain the earliest steady state cycle for this loading conditions is presented and discussed in detail in the following sections. The magnitudes of the applied pressure to the inner upper surface of the bush in cosine distribution formulation are calculated using Equation (1) such that the total load applied becomes equal to that of the experimental conditions.

$$p(\theta) = \frac{4L}{dt\pi}\cos\theta \quad (1)$$

where $p$ is the pressure in cosine distribution, $L$ is the maximum applied load which is provided in Table 2.2 for all specimens, $d$ is the internal diameter of the bush, and $t$ is the thickness.

The magnitudes of the applied cosine distributions during the simulations are presented in Table 3.1.

Table 3.1. Magnitudes of the applied pressure distributions in cosine form for each lug and bush combination.

| **Specimen** | Al lug – Al bush | Al lug – steel bush | Ti lug – steel bush |
|---|---|---|---|
| **Magnitude of the applied pressure distribution in cosine form [MPa]** | 76 | 111 | 306 |

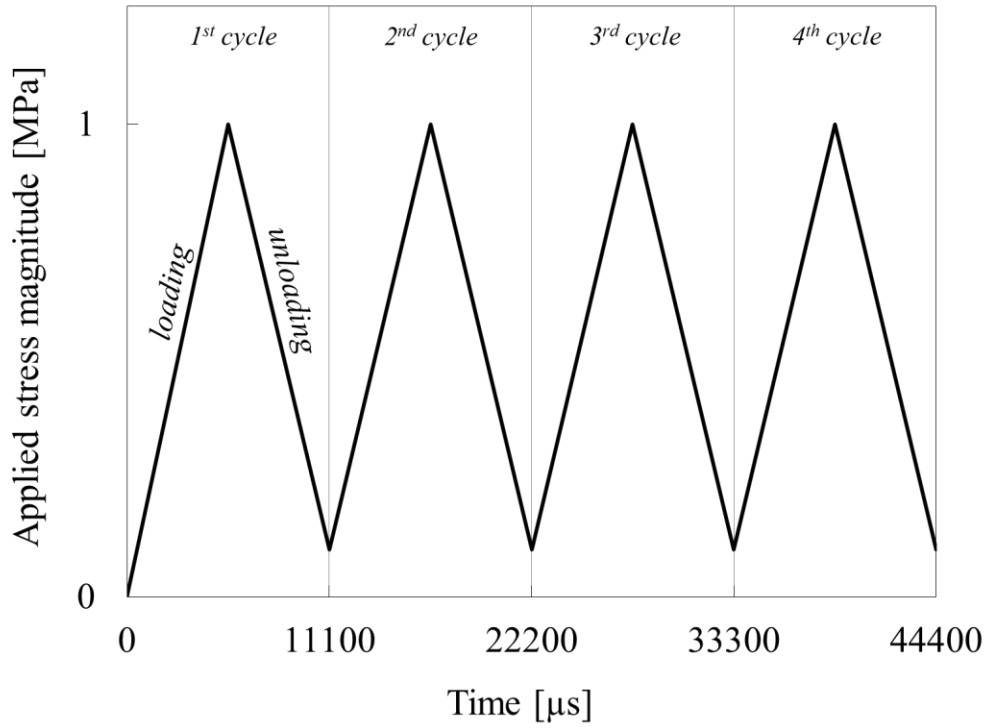


Figure 3.2. Normalized applied cyclic pressure at the 2nd step of the solution.

*Global and local coordinate systems*

In contact problems, ABAQUS defines local directions on the contact surfaces in order to present the outputs such as contact stresses, forces, and relative slip along these local directions [19].

A local coordinate system is defined for each element throughout the contact surface and is oriented by considering the outward surface normal of the element and the global coordinate system. In the local coordinate system, the local 1- and 3-directions correspond to the projection of the global x-direction onto the surface and the outward surface normal, respectively. The local 2-direction is then determined by considering the local 1- and 3-directions such that they form a right-handed coordinate system together. However, if the global x-direction is perpendicular to the contact surface at any location, then the global z-direction is assigned as the local 1-direction at that location. In such a case, the local 1-axis changes its direction in some regions leading to misrepresentation of the contact outputs. Therefore, in

contact problems, especially the ones with circular contact areas, the global coordinate system should be defined properly.

Figure 3.3 shows the local 1-direction of the contact elements around a cylinder. In some elements where the global x-direction is perpendicular to the contact surface, the local 1-direction is assigned as the projection of global z-direction, instead of global x-direction.

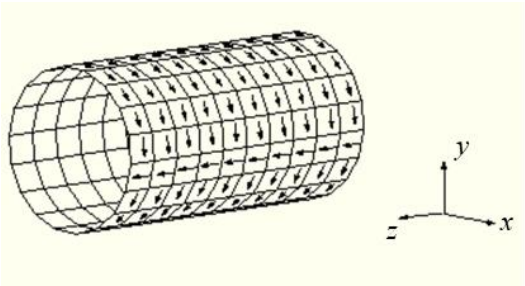


Figure 3.3. Default local 1-direction in ABAQUS. [19]

In this study, global x-direction corresponds to the transverse direction of the circular contact surface of the lug and bush in order to avoid any inconsistency about the local directions. In this way, the local 2-direction is circumferential and the local 1-direction is transverse.

## 3.2 Contact algorithm

The aim of the finite element model created is to simulate the experimental conditions as accurately as possible in four cycles and to understand the mechanisms occurring at the contact area between the lug and the bush. Therefore, a contact between the inner surface of the lug and the outer surface of the bush is modeled using master-slave algorithm. Contact area of the lug is considered as the master surface as shown in Figure 3.2-(b). Surface-to-surface contact discretization method with finite sliding contact tracking approach is followed. Tangential behavior of the contact between the master and slave surfaces is modeled with the simple Coulomb friction model using penalty approach, which is shown in Figure 3.4(b). The ideal

Coulomb friction law is shown in Figure 3.4(a). The ideal formulation does not allow contacting surfaces to slide unless the present shear stresses at the contact reach the critical shear stress, which is calculated by the multiplication of normal contact stresses and the friction coefficient. During sliding, the relative sliding distance, $\gamma$, increases while the shear stresses at the contact region is equal to the critical shear stress value. However, in the penalty formulation of Coulomb law, the relative sliding increases when the surfaces are sticking. The amount of slip experienced until the critical shear stress is reached is called elastic slip and is equal to 0.5% of the critical element length of the contact region by default in ABAQUS [19]. After reaching the critical shear stress, relative sliding increases while the shear stress stays equal to the critical shear stress value. If unloading starts at some point during sliding, the shear stresses will start to decrease, and the surfaces will stick until the negative critical shear stress is reached. During this sticking period, elastic slip will be observed which is the double of the elastic slip in first loading case, since the stiffness of the curves during elastic slip is equal and the amount of stresses that need to be covered in order to slide in reverse direction is two times of the 1st loading case.

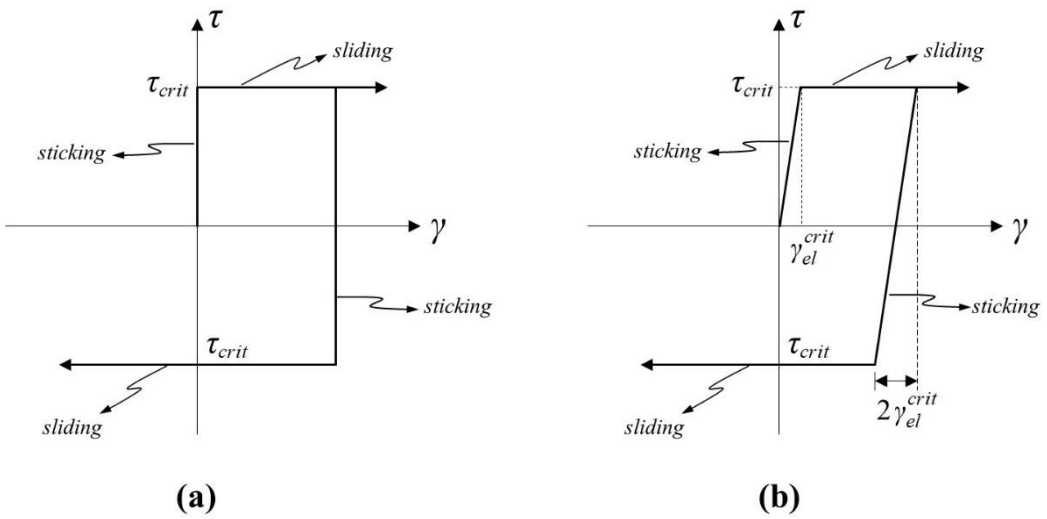


Figure 3.4. Coulomb friction model showing (a) idealized shear vs. relative sliding behavior and (b) penalty approach.

Two different friction coefficient values are defined for the contact of each material combination. After obtaining the static friction coefficient values from the literature for each material combination as 1, 0.6, and 0.6 for Al-Al, Al-steel and Ti-steel, respectively, one more friction coefficient value, which is 0.8 for each material combination and 1.2 additionally for Al-Al case, is defined in order to investigate the effect of changing friction coefficient. The higher friction coefficient values are intentionally selected higher since the friction coefficient value of the contact tends to increase during a fretting cycle [22].

### 3.3 Mesh convergence study

The finite element model is meshed at four different mesh densities: using 6212, 15584, 50770, and 81572 elements. Each model is simulated at the same conditions and for each model, both the maximum von Mises stress value at the lug and the maximum contact pressure value at the lug mating surface are compared.

Figure 3.5 shows the maximum von Mises stress value reached at the lug for four different models having different sized meshes. As the number of elements increases, the maximum stress observed at the lug converges to a value around 101.6. The increase in the maximum stress is less than 0.19% when the models with 50770 and 81572 elements are compared.

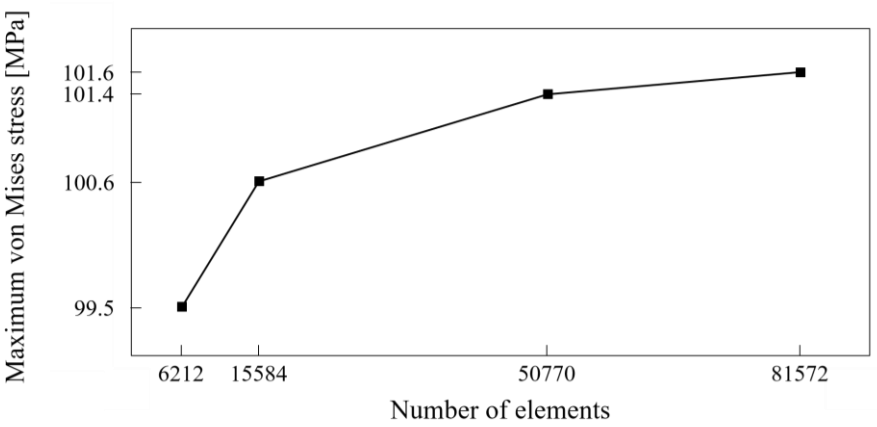


Figure 3.5. Maximum von Mises stress value at the lug at four models having different number of elements.

Similar to the mesh study on maximum von Mises stresses on four different mesh sizes, the maximum contact pressure at the contacting lug surface also converges to a value of 47.2 as the number of elements increases (). If the models with 50770 and 81572 elements are compared, the maximum contact pressure value increases 0.21%.

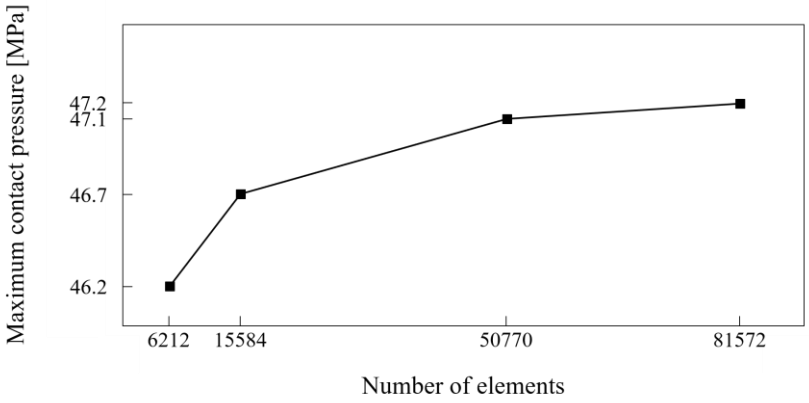


Figure 3.6. Maximum contact pressure value at the lug mating surface at four models having different number of elements.

The abovementioned mesh study shows that this model reaches convergence at a mesh density having 50770 elements. However, the finest model including 81572 elements is used to be on the safe side, for the rest of this study.

### 3.4 Fatigue damage parameters

There are several damage parameters in order to assess the fretting fatigue performance. These parameters predict the location of fretting crack initiation as a basis for the crack initiation lifetime assessments. Most of the parameters used in the fretting fatigue performance predictions are multiaxial fatigue criteria following the critical plane approach. The other types of approaches of the multiaxial fatigue criteria which are energy-based or static yield criteria are insufficient for the predictions in a fretting fatigue problem since they are not appropriate for the out-of-phase and non-proportional loading cases. Furthermore, among the three different critical plane approaches, stress-strain based models are able to reflect the constitutive behavior of the material and the cyclic hardening due to non-proportional loading [23,24]. Therefore, two stress-strain based multiaxial fatigue damage criteria will be used in this paper in order to predict the fretting crack initiation locations, namely Fatemi-Socie (FS) and Smith-Watson-Topper (SWT) parameters.

#### 3.4.1 Fatemi-Socie (FS) parameter

FS parameter is an energy-based critical plane approach and is suitable to cases where the initial crack growth occurs under Mode-II [23,25]. The parameter is expressed as a function of maximum shear strain amplitude $\Delta\gamma_{max}/2$ and the maximum normal stress $\sigma_{n,max}$ acting on the critical plane where shear strain amplitude is maximized as

$$FS = \frac{\Delta\gamma_{max}}{2}\left(1 + k\frac{\sigma_{n,max}}{\sigma_y}\right) \tag{2}$$

where $\sigma_y$ and $k$ are the monotonic yield strength and material constant found from the data of fatigue experiments, respectively. The material parameter $k$ is shown to have no effect on the predicted fretting crack locations [26]; therefore, will be assumed as 1. According to FS parameter, the fretting crack initiates at the location

where it is maximized. The critical plane at the initiation location corresponds to the initial crack plane.

### 3.4.2 Smith-Watson-Topper (SWT) parameter

SWT parameter is also an energy-based critical plane approach for the cases where the initial crack growth occurs under Mode-I [25]. The SWT parameter can be defined as the maximum of the product of normal strain amplitude $\Delta\varepsilon$ and maximum normal stress $\sigma_{n,max}$ as

$$SWT = \left(\sigma_{n,max}\frac{\Delta\varepsilon}{2}\right)_{max} \quad (3)$$

This formulation is a simplified version of the first SWT parameter for the cases of non-proportional loadings, like fretting, which gives the same results with greater simplicity [25]. Similar to the FS, the fretting crack initiates at the location where SWT parameter is maximized. The critical plane at the initiation location corresponds to the initial crack plane.

# CHAPTER 4

# NUMERICAL RESULTS AND DISCUSSIONS

## 4.1 Investigation of Al-Al lug-bush member

In this section, the events occurring at the contact surfaces of the Al lug and Al bush are described in detail in order to understand the type and sequence of the contact mechanisms under cyclic loading. For this purpose, the numerical results of the Al-Al lug-bush member simulating four full cycles with a stress ratio of $R = 0.1$ are presented. The applied load to the Al-Al lug-bush member during four cycles is shown in Figure 4.1. It is important to note that a distributed pressure is applied to the inner upper half surface of the bush in cosine form, as mentioned in Section 3.1. The corresponding load values are calculated using Equation (1). The letters on the applied load graph shown in Figure 4.1 shows the load and time values corresponding to the sticking-sliding states shown in Figure 4.3 during the loading of the 1$^{st}$ and 2$^{nd}$ cycles and unloading of the 1$^{st}$ cycle.

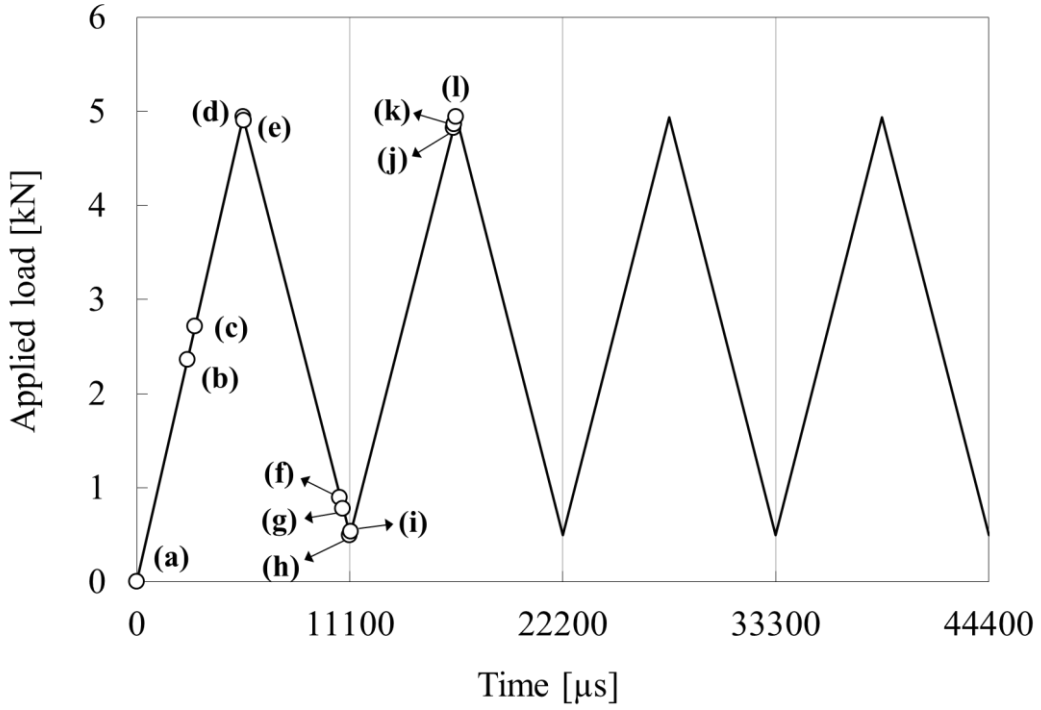


Figure 4.1. Applied load vs. time graph of Al-Al lug-bush member. The load is applied to the bush inner surface as pressure in cosine form, where the maximum applied pressure of 76 MPa corresponds to a maximum applied load of 4939 N. The letters show the time and load values of sticking-sliding states shown in Figure 4.3.

In the simulations, the effect of friction coefficient is investigated using two different friction coefficients, $\mu = 0.8$, $\mu = 1$. An additional simulation where the friction coefficient $\mu = 1.2$ is conducted and the results showed that sliding does not occur, and the mating surfaces stick together throughout the 4 cycles; the results of this simulation will not be shown here. Since the stress ratio is 0.1, the loading in the first cycle is not identical with the following cycles; therefore, the mechanisms observed during the 1st cycle are expected to be different than that of the following cycles. In order to obtain the number of cycles required to reach a steady-state response, each cycle is compared in terms of following aspects: (i) general load vs. displacement behavior, (ii) evolutions of the sticking and sliding regions during loading and unloading, and (iii) relative sliding distance experienced by a node on the bush mating surface. The observations on these three aspects shows that the steady state response is reached during the second cycle. In fact, the response during the

unloading of the first cycle is observed to be repeating during the unloading of the following cycles.

The steady state response can be observed at the load-displacement curve of Al-Al lug-bush member having a friction coefficient of $\mu = 1$ which is shown in Figure 4.2. The loading and unloading curves are almost identical throughout the four cycles, except the loading of the 1st cycle. Therefore, the load-displacement curve shows that the earliest steady-state response is obtained during the 2nd cycle.

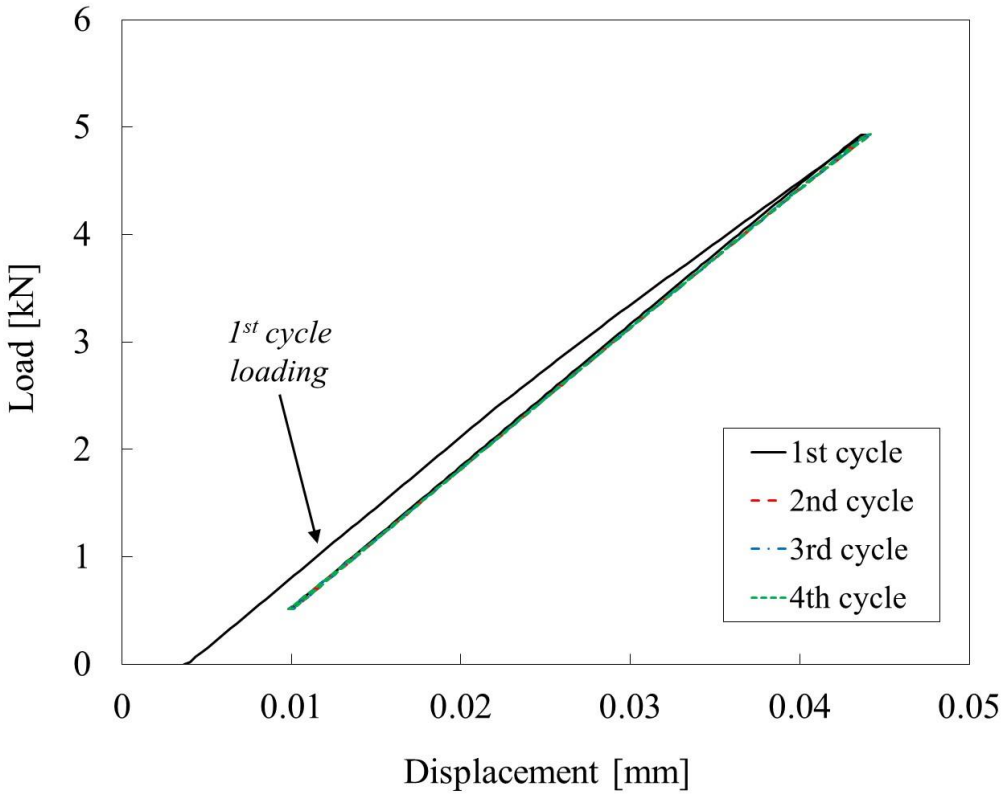


Figure 4.2. Load vs. displacement data of Al-Al lug-bush member during 4 cycles where the friction coefficient is 1. The displacement data is obtained at a node resting at the edge of lug mating surface where θ = 0°.

The steady state response, which is reached during the 2nd cycle, is also observed in the relative sliding distance-time curves as shown in Figure 4.4 and in the evolution of sticking and sliding regions. For simplicity reasons, sliding evolutions are

presented during only the 1st cycle, and loading of the 2nd cycle, as shown in Figure 4.3.

The sticking-sliding states observed on the lug mating surface when $\mu = 1$ are shown in Figure 4.3(a)-(d) during the loading of the 1st cycle, in Figure 4.3(e)-(h) during the unloading of the 1st cycle, and in Figure 4.3(i)-(l) during the loading of the 2nd cycle. The sticking-sliding states are identical at the right- and left-hand sides of the lug and bush mating surfaces. Therefore, only the left-hand-side of the lug mating surface is shown.

At the beginning of the loading, lug and bush mating surfaces stick to each other initially (Figure 4.3(a)) since the tangential forces at these surfaces cannot yet overcome the friction force according to the Coulomb's Law. As the applied load increases, sliding initiates at 2550 μs at the thickness-wise edges of the lug mating surface at an angle of 116° and then these sliding regions meet at the mid-thickness at 2700 μs. Figure 4.3(b) shows the sticking-sliding state at 2650 μs, just before the union of edge sliding regions at the mid-thickness. Further increase in the applied load widens the sliding region in both $+\theta$ and $-\theta$ directions, as shown in Figure 4.3(c). When the applied load reaches its maximum value at 5550 μs, the sliding region also reaches its widest boundaries which are between 80° and 171°, as shown in Figure 4.3(d).

As soon as unloading starts, the state of the lug mating surface turns into sticking state completely (Figure 4.3(e)). Upon unloading, a similar evolution to that of loading is observed. Initially, the mating surfaces preserve their sticking state. At 10450 μs, small sliding regions initiate at the edges of the lug mating surface at an angle of 122°. Further unloading enlarges these edge sliding regions before they unite at the mid-thickness, as shown in Figure 4.3(f). At 10750 μs, these sliding regions grow and meet at the mid-thickness, 300 μs after their initiation (Figure 4.3(g)). As the loading decreases further, sliding region grows both in $+\theta$ and $-\theta$ directions and at the end of unloading at 11100 μs, reaches its widest boundaries, between 114° and 133° (Figure 4.3(h)).

At the beginning of the 2nd cycle, the mating surfaces stick to each other immediately (Figure 4.3(i)). Small sliding regions initiate at the edges at 16450 μs and grows with further loading as shown in Figure 4.3(j). These sliding regions first meet at the mid thickness, grow both in $+\theta$ and $-\theta$ directions, and then reach the widest boundaries at the end of one-half cycle which are 114° and 133° (Figure 4.3(l)), similar to the evolutions observed in the loading and unloading of the 1st cycle.

During the cyclic loading, the maximum sliding region areas are reached at the end of one-half cycles; however, the maximum extent of the sliding region during the loading of the 1st cycle is greater than that of other two one-half cycles as observed in Figure 4.3. The location and extent of the maximum sliding regions are observed to be the same at the rest of the cyclic loading, except the loading of the 1st cycle.

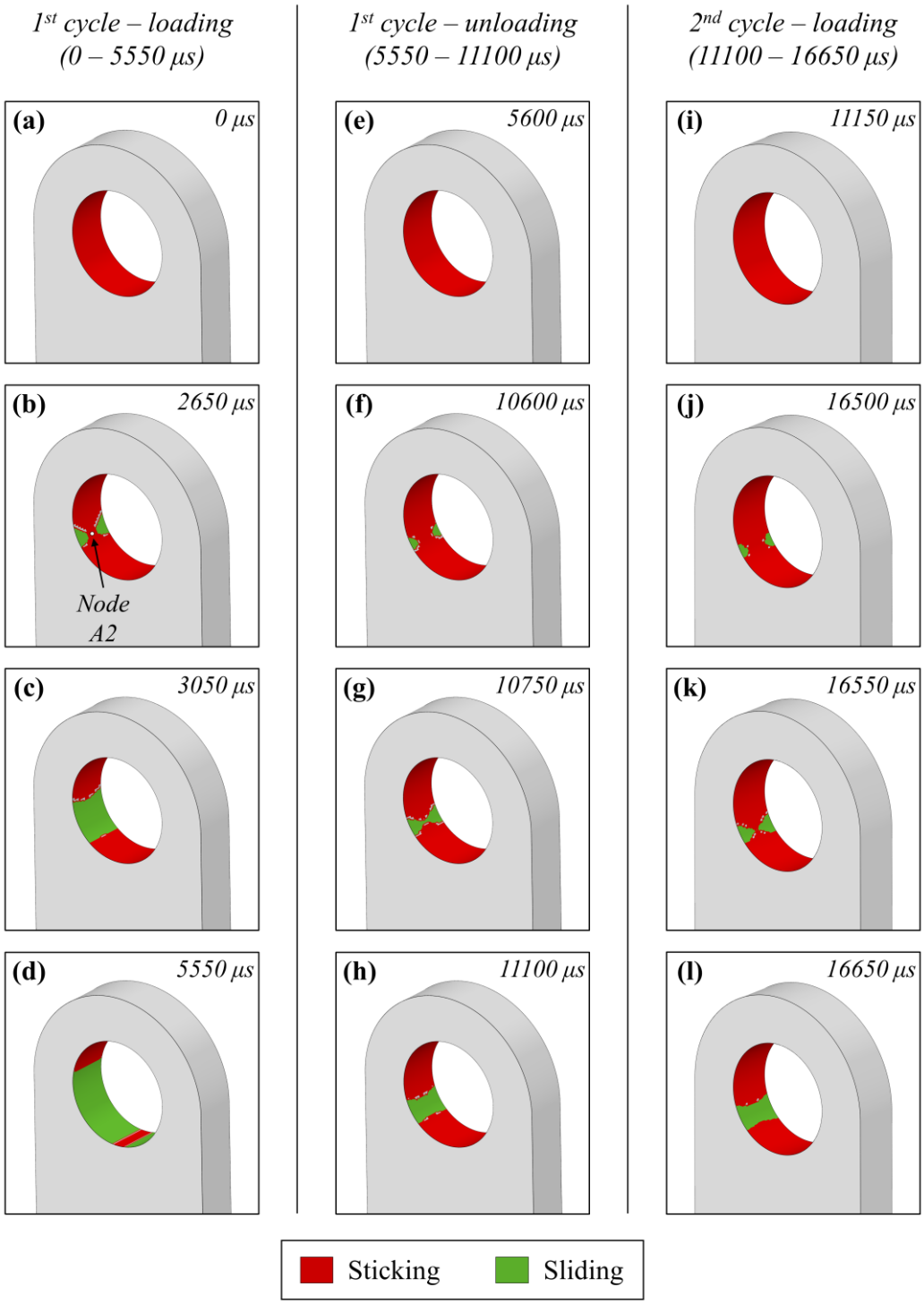


Figure 4.3. Evolution of sticking and sliding regions shown on the lug mating surfaces of Al-Al lug-bush member having a friction coefficient of 1 during (a)-(d) loading of the 1st cycle (0 – 5550 μs), (e)-(h) unloading of the 1st cycle, and (i)-(l) loading of the 2nd cycle. Sticking and sliding regions are represented with red and green, respectively.

Figure 4.4 shows the relative sliding distance of a particular node, node A1, which rests at the mid-thickness of the bush mating surface where the sliding initiates during the loading of the 1st cycle. Since the node is located at the mid-surface, the relative sliding in the thickness-wise direction is negligible when compared to the relative sliding in circumferential direction. Hence, only the relative sliding distance in the circumferential direction is considered. In Figure 4.4, the y-axis of the graph shows the relative sliding distance between the node A1 on the outer bush surface and its mating node at the undeformed state, node A2, on the inner lug surface which is shown in the Figure 4.3(b). Relative sliding distance of node A1 during the four cyclic loading of Al-Al lug-bush member having a friction coefficient of 1 is shown with black line in Figure 4.4. Black square markers on this curve indicate the times in which node A1 starts to slide at each one-half cycle when $\mu = 1$. It is worth to note that the first sliding at the contact area initiates before the sliding of the Node A1, as shown in Figure 4.3. The red line and the red square markers show the results of Al-Al lug-bush member having a friction coefficient of 0.8. Starting from the 2nd cycle, the relative sliding behavior reaches a steady-state, and the response of the 2nd cycle is repeated in the following cycles. The black dashed line and the circular marker show the results of Al-Al lug-bush member having a friction coefficient of 1.2. In this case, sliding is observed only during the loading of the 1st cycle. As the unloading starts, sliding vanishes and is not observed in the following cycles. Therefore, the relative sliding behavior of this case exhibits only the elastic slip except the loading of the 1st cycle.

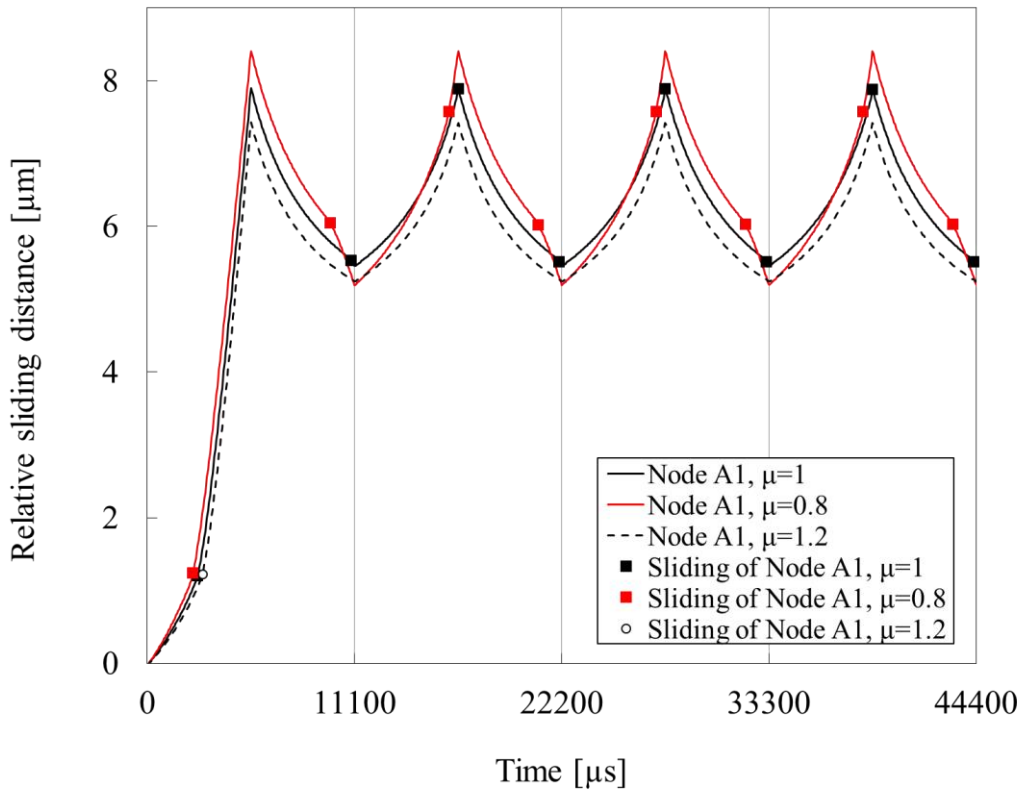


Figure 4.4. Relative sliding distance vs. time data of Al-Al lug-bush member obtained at node A1 at three different friction coefficient values: 0.8, 1, and 1.2. Black and red square markers at each one-half cycle indicate the times in which node A1 starts to slide when friction coefficient is 1 and 0.8, respectively. Black circle shows the time in which Node A1 starts to slide during the loading of the 1st cycle only, when friction coefficient is 1.2.

In both the $\mu = 1$ and $\mu = 0.8$ cases, the mating surfaces stick to each other at the beginning of the loading. During this sticking period, one would normally expect that the relative sliding distance of any node should be zero; however, penalty friction formulation enforces the mating surfaces to have some amount of slip for easy convergence, which is called *elastic slip*. As the loading increases, node A1 starts to slide with respect to node A2 as shown with black and red square markers for $\mu = 1$ and $\mu = 0.8$ cases, respectively. Starting from that point, the relative sliding amount increases rapidly. When the loading ends and the maximum applied stress magnitude reaches 76 MPa, the relative sliding amount of node A1 reaches a maximum value of 7.9 μm and 8.4 μm for $\mu = 1$ and $\mu = 0.8$ cases, respectively. In

the unloading cycle, an initial elastic slip is observed while the mating surfaces are sticking, similar to the loading. Upon further unloading, node A1 starts sliding at the times indicated with square markers and the amount of relative sliding decreases in which the sliding direction is the opposite of the direction in the loading. At the end of the unloading cycle at 11100 μs, where the applied pressure is decreased to 10% of the maximum value since $R = 0.1$, the relative sliding does not return to its initial value of zero. Instead, a *residual slip,* $\gamma_r = 5.5\ \mu m$ and $5.2\ \mu m$ for $\mu = 1$ and $\mu = 0.8$ cases remain between the initial and final positions of the node A1 with respect to its initially mating node, node A2.

Comparison of both $\mu = 1$ and $\mu = 0.8$ cases shows that, in the lower friction coefficient case, the maximum relative sliding distance is greater than the higher friction coefficient case. Sliding of Node A1 also initiates earlier in lower friction coefficient case which results in greater sliding areas at the ends of each one-half cycle.

The elastic slip amount experienced at the beginning of the loading in the 1st cycle of $\mu = 1$ case is around 1.2 μm as can be seen in Figure 4.4, which is equal to 0.5% of the characteristic element length at the contact region [19]. However, during the following one-half cycles, the elastic slip amount doubles and reaches to approximately 2.4 μm. The reason for that difference is the reversals of shear stress direction. Since the loading of the 1st cycle does not have residual stresses resulted from the previous cycles, the amount of change in the shear stresses in order to reach the critical shear stress and initiate sliding causes 1.2 μm of elastic slip. However, as the loading ends and unloading starts, the residual shear stresses decrease to zero first, then decrease further and reach critical shear stress value which is the negative of the loading case. The amount of change in the shear stresses in order to reach the negative critical shear stress is the two times of the 1st loading case and causes higher elastic slip, which is the double of the observed value in the 1st loading case. Figure 3.4 summarizes this phenomenon with a shear stress vs. total slip curve.

Figure 4.5 shows the relative sliding distance and slip rate of the Node A1 of Al-Al lug-bush member during four cycles having a friction coefficient of 0.8. In order to observe the changes in relative sliding distance and slip rate clearly after the sliding of Node A1, the results obtained when the friction coefficient is 0.8 are used in Figure 4.5. In the case where friction coefficient is 1, the Node A1 starts to slide just before the end of each one-half cycle; therefore, the changes in relative sliding distance and slip rate cannot be observed clearly.

Node A1 rests at an angle where sliding initiates; however, sliding initiation starts from the edges and the Node A1 is located at the mid-thickness. Therefore, the times of the first sliding and the sliding of Node A1 is not the same but very close to each other, as shown with the dashed lines and circular markers, respectively, in Figure 4.5. Before the initiation of the first sliding, every point on the contact region experiences elastic slip. When first sliding initiates at the edges, slip rate of Node A1 increases rapidly (almost linearly) even though the Node A1 is not sliding yet. After the sliding region reaches to Node A1, slip rate of this node increases with a decreasing slope and approaches to a constant slip rate value. However, before the slip rate reaches to a constant value, one-half cycle ends. At the ends of each one-half cycle, the sign of the slip rate changes.

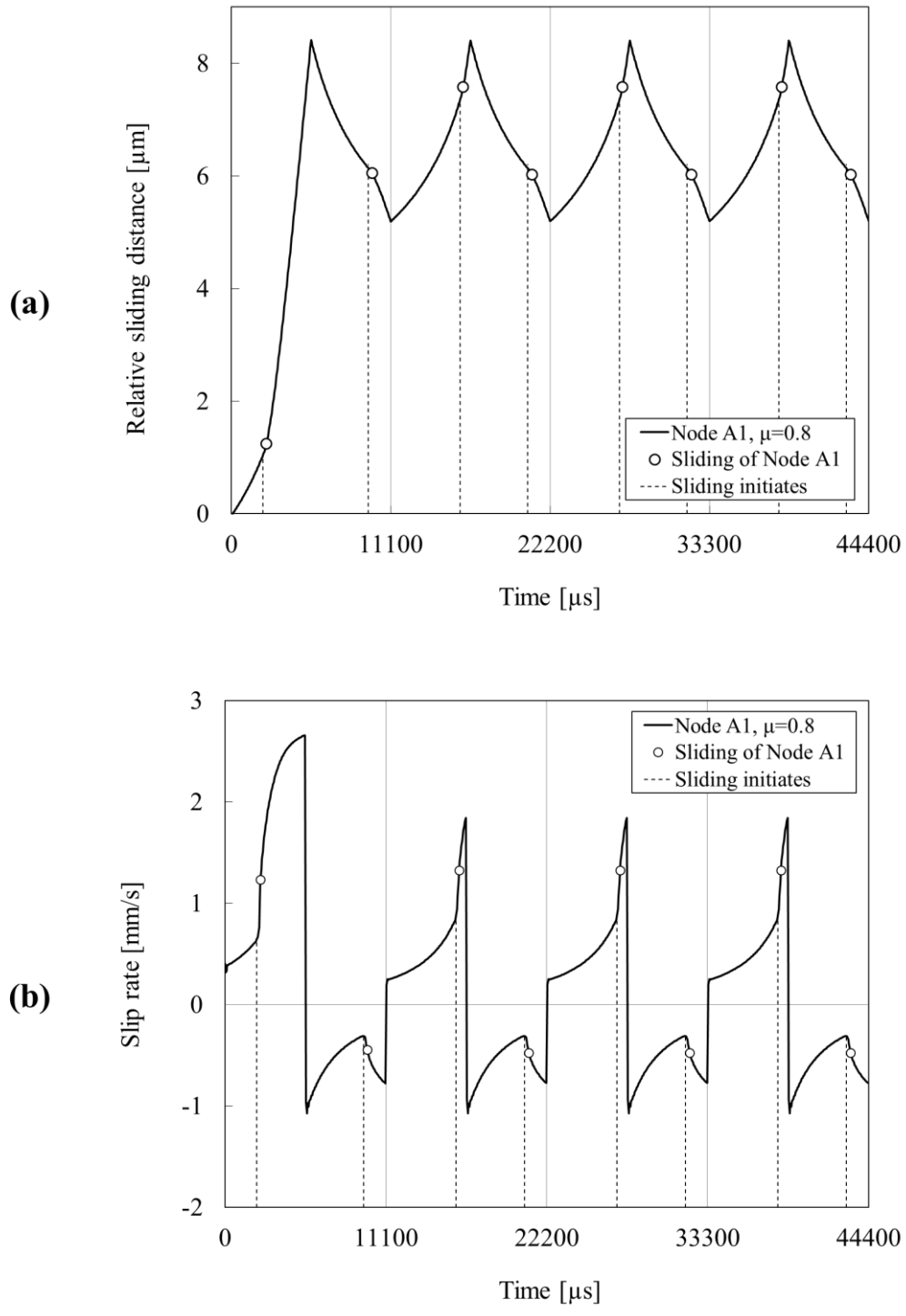


Figure 4.5. (a) Relative sliding distance and (b) slip rate of the Al-Al lug-bush member having a friction coefficient of 0.8 during four cycles. Dashed lines show the times in which the first sliding at the contact area initiates. The circular markers indicate the initiation of sliding times of Node A1.

The evolution of shear tractions at the lug mating surface, when the friction coefficient is 1, during the loading of the 1st cycle, unloading of the 1st cycle, and loading of the 2nd cycle is shown in Figure 4.6(a), (b), and (c), respectively, at discrete times. The shear tractions are obtained along a path at the mid-thickness of the lug mating surface of Al-Al lug-bush member, where 0° corresponds to the top of the lug, and show the shear stress distributions in the circumferential direction. Since the path followed is located at the mid-thickness, the shear stresses in the thickness-wise direction is negligible and the shear stresses in circumferential direction is almost equal to the equivalent shear tractions. Therefore, only the shear tractions in circumferential direction are considered here. The left and right square markers of each line represent the upper and lower boundaries of the sliding region at the corresponding time. The shear distributions at the ends of each one-half cycle are shown with red lines. In Figure 4.6(b) and (c), the shear distributions at the beginning of the half cycles are shown with black dashed lines and these lines are the same with the end-state distribution of the previous half-cycle which was shown in red.

At the beginning of the loading during the 1st cycle, the shear stresses along the path are nearly zero. As the loading increases, the magnitude of the shear stresses also increases. The sign of the shear stresses changes along the path such that the shear stresses are positive at the bottom parts and negative at the upper parts. Shear stresses at the bottom parts, where $\theta$ is greater than approximately 90°, increase as the loading increases until the initiation of sliding. As the shear traction at any node reach the critical shear stress value, which is equal to the multiplication of normal traction of that node and the friction coefficient, the node starts to slide. In 2700 μs, sliding initiates and as the loading increases, sliding region widens. During sliding, shear traction is restricted by the critical shear stress value which decreases in this problem as the applied load is increased since the normal tractions at the bottom parts of the lug decrease upon loading. During the loading of the 1st cycle, two local peaks occur in the shear traction distribution as sliding develops and the sliding region falls between these local peaks.

As the loading of the 1st cycle ends and unloading starts, the end-state shear stress distribution of the of 1st cycle becomes the residual for the unloading. Upon unloading, the shear stresses at the bottom part decreases and in order for a node to start sliding, the shear stresses should decrease to negative values first and then reach the negative critical shear stress. During unloading, shear stresses along the path reach the critical shear stress values 350 μs before the end of unloading and as the sliding region grows, the magnitude of the shear stresses at these regions increases. The magnitude of the shear stresses in the sliding regions are greater in the unloading of the 1st cycle when compared with the loading since the normal stresses increase during unloading and therefore, the critical shear stress values also increase.

Similar to the unloading of the 1st cycle, the loading of the 2nd cycle starts with residual shear stresses which are the end-state of the previous one-half cycle. Shear stresses at the bottom part increases as loading increases and reach the critical shear stress value resulting in the initiation of sliding.

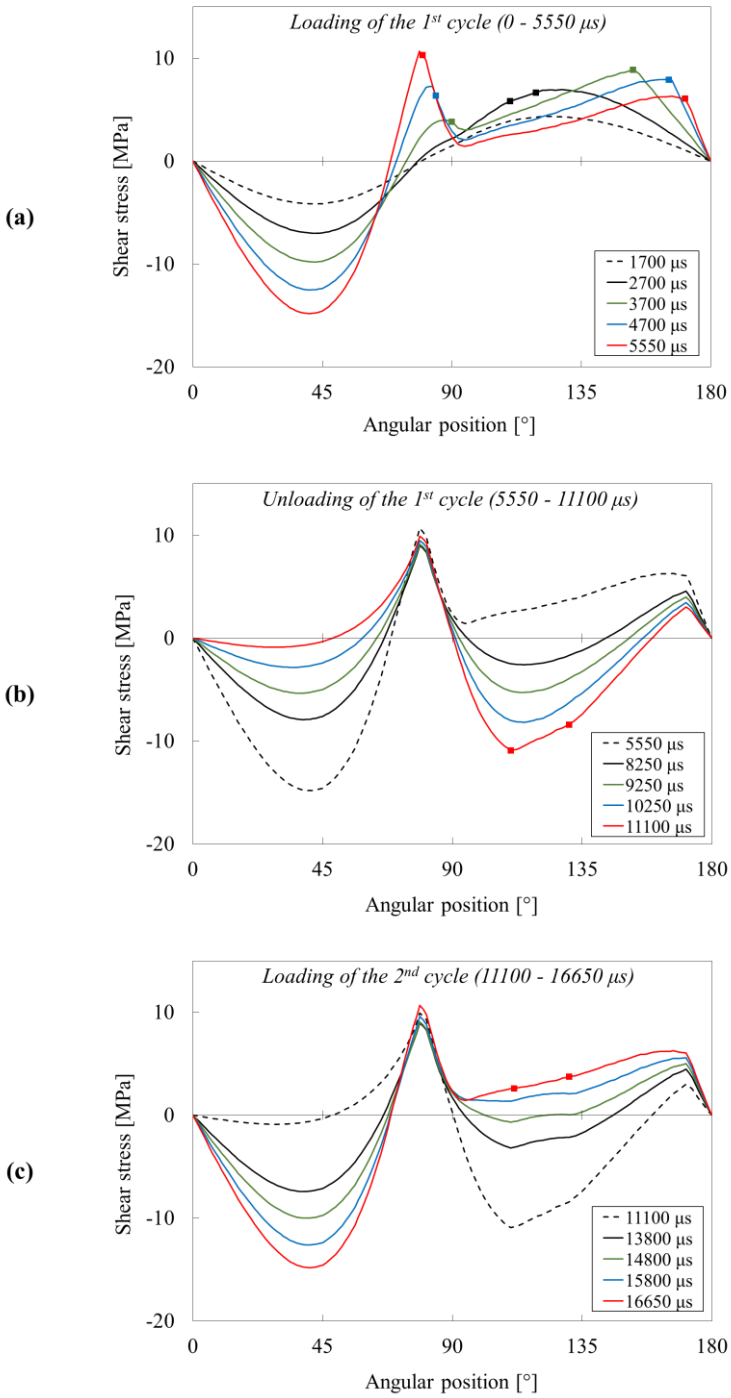


Figure 4.6. Shear stress distributions along a path taken at the mid-thickness of the lug mating surface, where top of the lug is 0°, during (a) loading of the 1st cycle, (b) unloading of the 1st cycle, and (c) loading of the 2nd cycle of Al-Al lug-bush member having a friction coefficient of 1. The left and right square markers located on each line indicate the upper and lower boundaries of the sliding regions at corresponding times, respectively.

When the loading of the 1st and 2nd cycles are compared, the evolution of shear stresses exhibits differences, except the end-state shear stress distributions. Although the end-state of the shear stress distributions at the loading of the 1st and 2nd cycles looks very similar when Figure 4.6(a) and (c) are compared, the extent of the sliding regions at the end of these one-half cycles are very different. The sliding region obtained at the end of loading of the 2nd cycle is smaller than that of loading of the 1st cycle; it does not reach the local peaks observed in the shear stress distribution in contrast to the loading of the 1st cycle. However, when the shear tractions and critical shear stresses at the end of loading of the 2nd cycle are compared (see Figure 4.7), it can be observed that the shear tractions are almost equal to the critical shear stresses in the sticking regions between the local peaks. The minute difference between these two stress distributions prevents sliding at the right and left regions of the current sliding region.

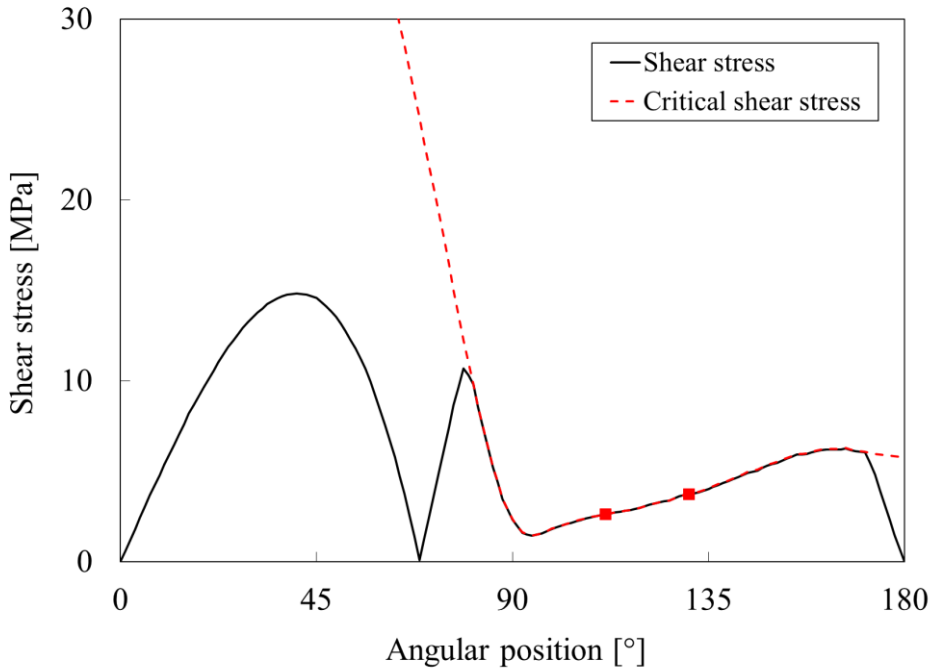


Figure 4.7. Resultant shear stress vs. angular position graph showing the shear stress and critical shear stress distributions along a path taken at the end of loading of the 2nd cycle and at the mid-thickness of the lug mating surface of Al-Al lug-bush member having a friction coefficient of 1. The left and right square markers indicate the upper and lower boundaries of the sliding region.

The observation raised the question of whether these sticking regions turns into sliding if the loading is continued. For this purpose, the simulation of the Al-Al lug-bush member having a friction coefficient of 1 is modified such that the loading continues during additional 600 μs after it reaches its previous maximum value at 16650 μs. The results show that the sticking regions start to slide immediately after 16650 μs, as shown Figure 4.8. The extent of the sliding region (Figure 4.8(d)) becomes the same as that of the loading of the 1st cycle in a very small time increment which is 1.7 μs. However, the evolution of sliding regions occurs differently when compared with the evolution of the sliding in the loading of the 1st cycle. During the loading of the 1st cycle, the sliding region initiated around 116° at the edges of the lug mating surface and then widened in both +θ and -θ directions until the end of loading. However, in the infinitesimal load increase case, the sliding region reached at 16650 μs stays invariably after 0.9 μs and new sliding regions initiate at approximately 80° and 171° (Figure 4.8(b)). Then, these newly developed sliding regions grow towards the existing sliding region (Figure 4.8(c)) and meet with that region approximately in 1 μs forming a continuous sliding region which lies between 80° and 171° (Figure 4.8(d)), which is the same with the sliding region boundaries observed in the loading of the 1st cycle. However, it should be noted that the sliding evolution occurs differently between the loadings of the 1st and 2nd cycles. The top newly developed sliding region shown in Figure 4.8(b) propagates 1.42 mm in 0.2 μs, as shown in Figure 4.8(c). The average speed can be calculated as 7100 m/s.

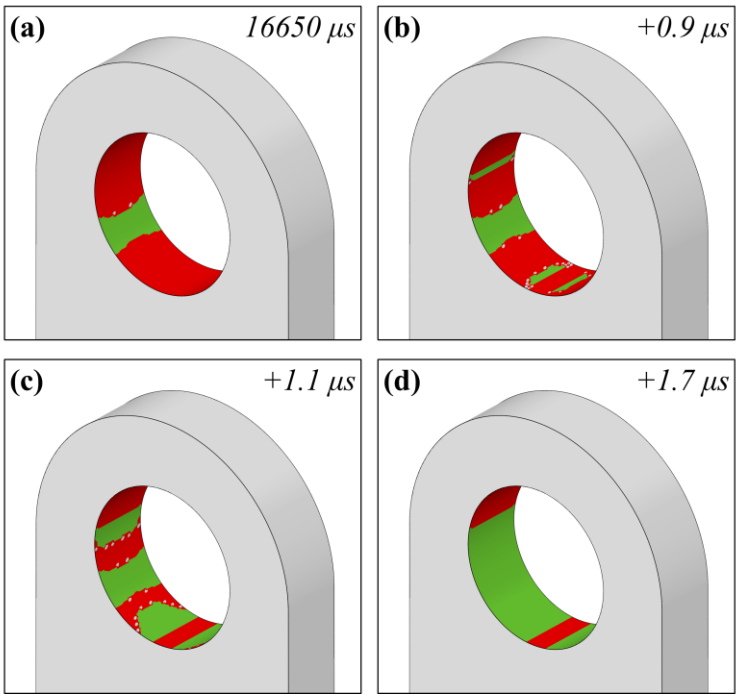


Figure 4.8. Evolution of newly developed sliding regions when the loading is continued after reaching its previous maximum value at 16650 μs in Al-Al lug-bush member having a friction coefficient of 1. Dynamic evolution of the sliding regions is presented (a) at 16650 μs, which is the state reached at the previous maximum load, and after (b) 0.9 μs, (c) 1.1 μs, and (d) 1.7 μs.

Figure 4.9 shows the location of sliding nodes during the 4 cycles in Al-Al lug-bush member having a friction coefficient of 0.8. Since the sliding starts at the last 350 μs and 100 μs of the loading and unloading during the 2$^{nd}$ and the following cycles, Figure 4.9 uses the results obtained when the friction coefficient is 0.8 in order to be able to show the slip front distance and speed graphs. In this figure, every sliding node along a path taken at the mid-thickness of the lug mating surface is illustrated with a dot. The uppermost and lowermost sliding nodes along the path at a time represent the upper and lower front of the sliding region at that time. Therefore, the upper and lower boundaries of the sliding region which are shown in Figure 4.9(a) with red and blue lines show the angular positions of the upper and lower slip fronts, respectively, with respect to time. The extent of the maximum sliding region is greatest at the loading of the 1$^{st}$ cycle. During the unloading of each cycle, sliding initiates earlier when compared to loading of the 2$^{nd}$ and the following cycles. The

steady state response reached during the 2nd cycle can be observed clearly in Figure 4.9(a). Therefore, Figure 4.9(b) shows the distance taken by the upper and lower slip fronts during only the loading and unloading of the 1st cycle and loading of the 2nd cycle. At this point, it is worth to note that the slip front distance should not be confused with the relative sliding distance. Slip front distances are covered by the fronts of the sliding regions while the relative sliding distance shows the relative position of a node on the outer bush surface with respect to its initially mating node on the lug inner surface. As shown in Figure 4.9(b), lower slip fronts cover greater distances when compared with the upper ones. This phenomenon is also observed analytically in axially pin-loaded lugs by Antoni [8]; the study shows that the distance covered by the lower slip front is always greater than that of upper one regardless of the axial load magnitude. In Figure 4.9(c), speeds of the upper and lower slip fronts are presented. Since greater distances are covered by the lower slip fronts when compared with the upper ones at the same time intervals, the speeds of lower slip fronts are greater. Towards the end of each half-cycle, slip front speed decrease rapidly. Since the slip fronts are not propagating continuously at the ends of half-cycles, speed distributions are not smooth.

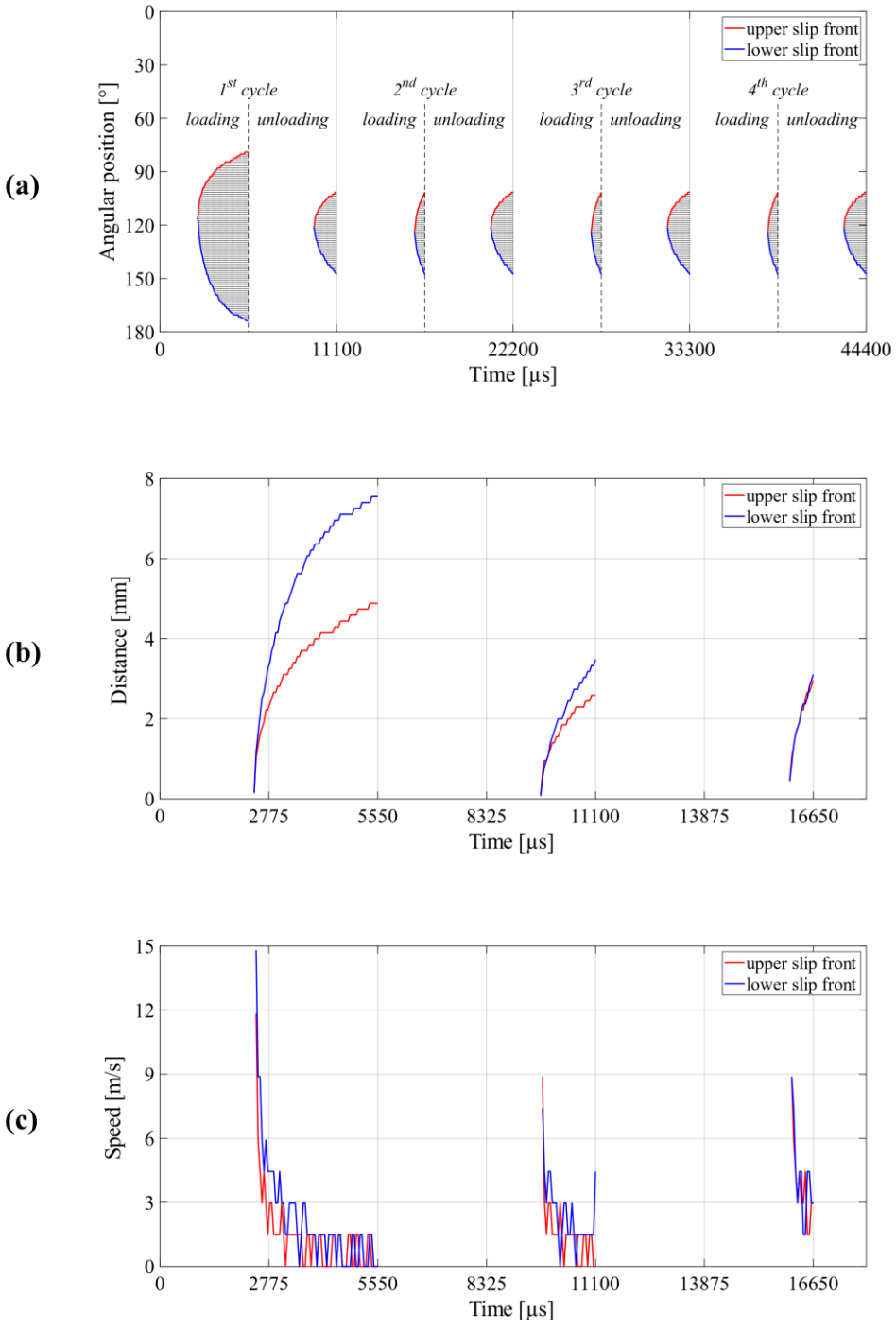


Figure 4.9. (a) Angular position vs. time graph showing the location of sliding nodes with black dots throughout the four cycles of Al-Al lug-bush member having a friction coefficient of 0.8. The upper and lower slip fronts are shown with red and blue curves. (b) Distance and (c) speed curves of the upper and lower slip fronts with respect to time during the loading and unloading of the 1st cycle and loading of the 2nd cycle.

The maximum sliding region areas reached during the loading of the 1st and 2nd cycles and unloading of the 1st cycle when the friction coefficient is taken as $\mu = 0.8$ and $\mu = 1$ are summarized in Figure 4.10(a). The maximum sliding region areas observed during the unloading of the 1st cycle and the loading of the 2nd cycle, and their locations are the same. During the loading of the 1st cycle, the extent of the sliding region is greater than the sliding regions of the following one-half cycles. If the friction coefficient is increased, the area of the maximum sliding region decreases in all one-half cycles as shown in Figure 4.10(a). If the load is increased infinitesimally at the same rate after reaching its maximum value, new sliding regions develop at both sides of the existing sliding region, as already shown in Figure 4.8. Then these new sliding regions propagate towards the existing sliding region and unite approximately in 2 μs.

The locations of tribolayer regions observed in the tested Al-Al lug-bush member are presented in Figure 4.10(b). The experimental observation of Al-Al lug-bush member show that the tribolayer regions are discontinuous along the mating surface and also unsymmetrical when LHS and RHS are compared. The discrete tribolayer regions observed at 100° an 90° at LHS and RHS, respectively, may be the result of infinitesimally higher loads occurring during the experiments than the prescribed maximum load levels. The infinitesimal increase in the load during the dynamic propagation of newly developed sliding regions, which takes approximately 2 μs, corresponds to approximately 2 N. In other words, a 0.05% increase in the maximum applied load can result in greater sliding regions initiating at different sites than the location of existing sliding region. Repetition of this infinitesimal over-loads may result in discrete tribolayer regions, as observed in the tested Al-Al lug-bush member (Figure 4.10(b)).

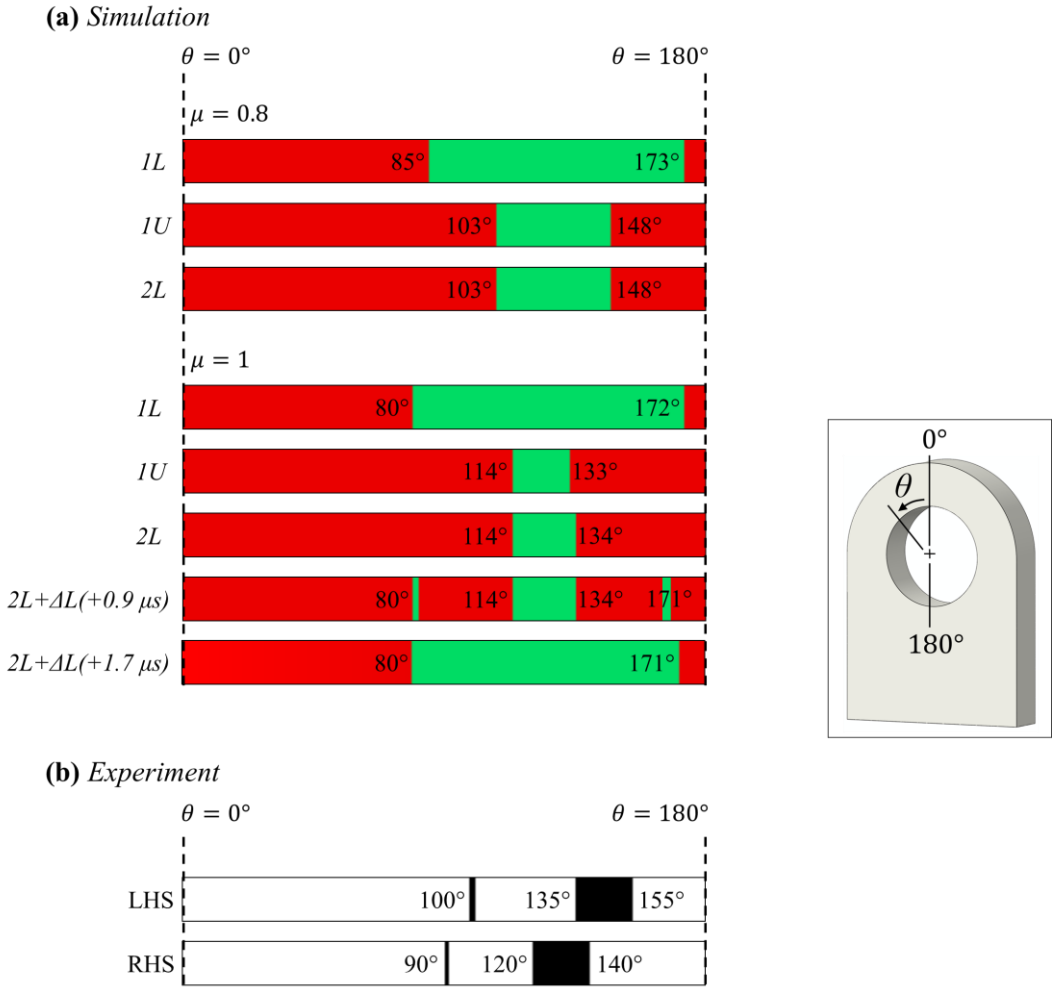


Figure 4.10. (a) Locations of the maximum sliding regions on the lug mating surface during loading of the 1st cycle (1L), unloading of the 1st cycle (1U), and loading of the 2nd cycle (2L) of Al-Al lug-bush member at two different friction coefficients (0.8 and 1). The sliding regions obtained by increasing the maximum load incrementally for the friction coefficient of 1 is also shown ($\Delta L_{+0.9\ \mu s}$ and $\Delta L_{+1.7\ \mu s}$). Sticking and sliding regions are represented with red and green, respectively. (b) Locations of the tribolayer observed on both LHS and RHS of the bush mating surface of tested Al-Al lug-bush member in which black represents the regions with tribolayer and white represents the clean regions.

## 4.2 Investigation of Al-Steel lug-bush member

The numerical results of the cyclic loading of Al lug and steel bush specimen with a stress ratio of 0.1 are presented in this section. Simulations are carried out using two different friction coefficient values which are 0.6 and 0.8 in order to investigate the effect of friction coefficient.

The applied load vs. time graph of the Al-steel lug-bush member is shown in Figure 4.11. The letters on the applied load graph shown in Figure 4.11 displays the load and time values of the sticking-sliding states shown in Figure 4.13 during the loading of the 1st and 2nd cycles and unloading of the 1st cycle.

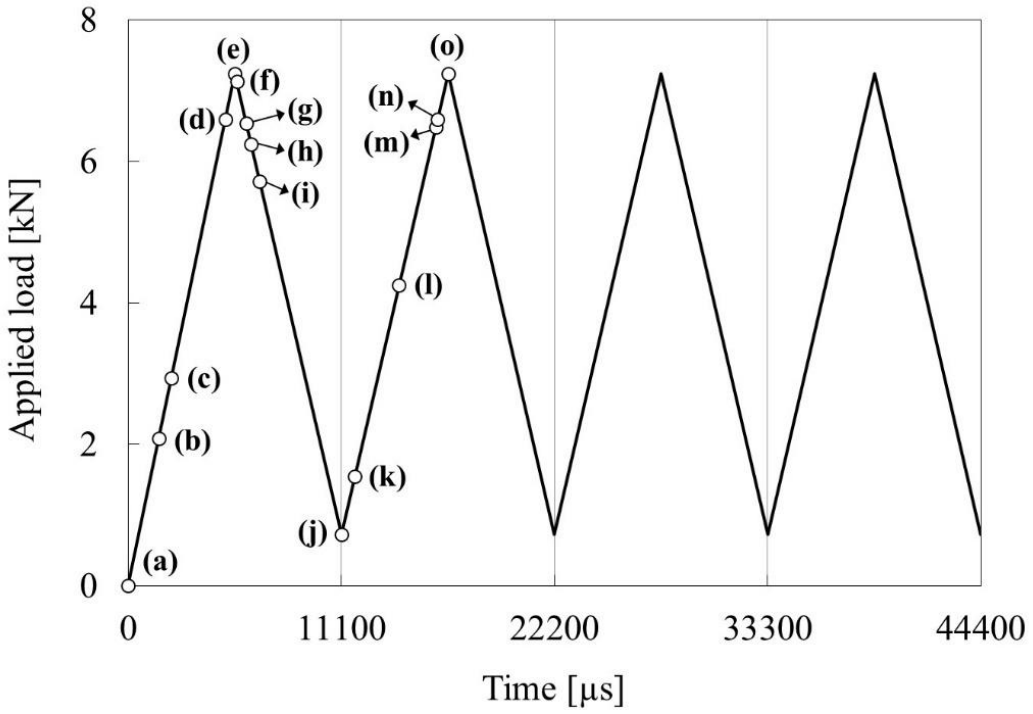


Figure 4.11. Applied load vs. time graph of Al-steel lug-bush member. The load is applied to the bush inner surface as pressure in cosine form, where the maximum applied pressure of 111MPa corresponds to a maximum applied load of 7244 N. The letters show the time and load values of sticking-sliding states shown in Figure 4.13.

The general behavior of Al lug and steel bush member with a friction coefficient of $\mu = 0.6$ under cyclic loading is shown in Figure 4.12. The x-axis shows the

displacement of a node at the mid- of the lug mating surface where $\theta = 0°$ and the y-axis shows the total applied force. The loading of the 1st cycle follows a different path than the loading of remaining cycles. The general behavior at the unloading of all cycles is identical. The loading and unloading paths of the 2nd cycle is identical with the loadings and unloading of the following cycles, separately, concluding that the earliest repeating cycle is the 2nd cycle, and it is identical to the 3rd and 4th cycles. These identical cycles experience hysteresis behavior since the paths taken during the loading and unloading are different.

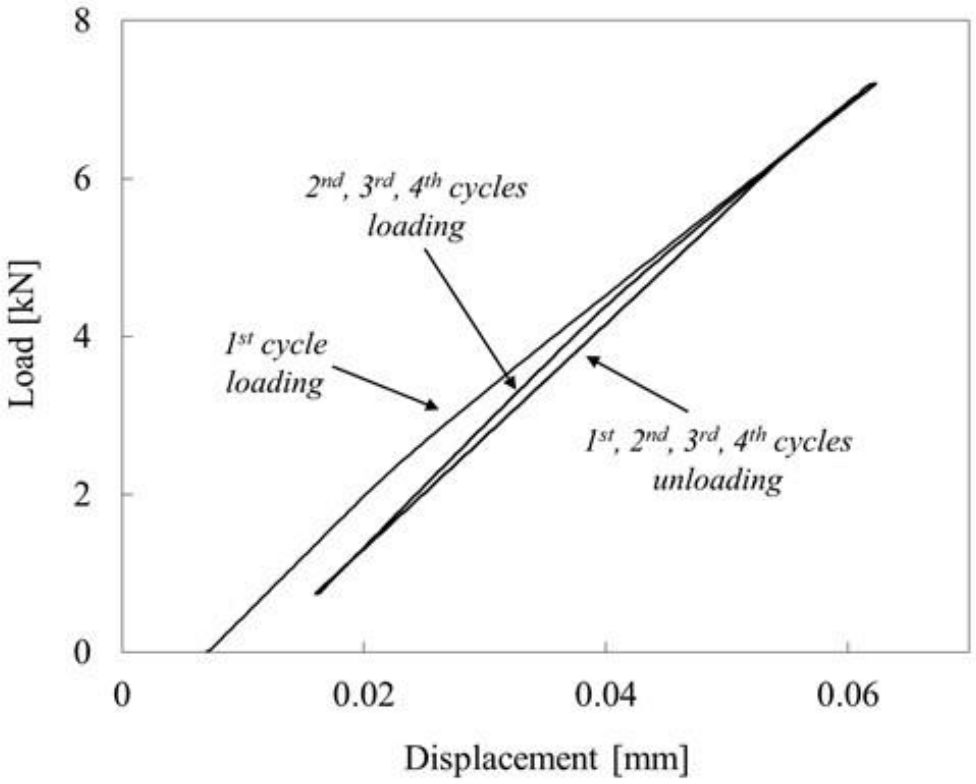


Figure 4.12. The load vs. displacement graph of the Al-steel lug-bush member ($\mu = 0.6$). The displacement data is obtained at a node resting at the edge of the lug mating surface where $\theta = 0°$.

Evolution of the sticking-sliding state at the lug mating surface of Al-steel lug-bush member having a friction coefficient of $\mu = 0.6$ during the loading and unloading of the 1st cycle, and loading of the 2nd cycle is summarized in Figure 4.13 in which the sticking, sliding, and opening regions are shown with red, green, and grey,

respectively. Sequence and type of events occurring at the contact region of Al-steel lug-bush member differ from the results presented in Section 4.1 for Al-Al lug-bush member. The main difference between the mechanisms of these two material combinations is the formation of opening at the contact region. In the results of Al-steel lug-bush member, an opening region initiates during the loading since the contact pressure at these regions drop to zero. As the applied load is increased, the opening region grows. When the loading ends and unloading starts, the opening region remains at the contact surface unlike the sliding regions and upon further unloading, it vanishes rapidly. The detailed evolution of the lug mating surface is presented in Figure 4.13.

At the beginning of the loading of the 1$^{st}$ cycle, lug and bush mating surfaces stick to each other initially (Figure 4.13(a)) as also observed in the Al-Al lug-bush member. As the applied load increases, sliding initiates at 1550 μs at the thickness-wise edges of the lug mating surface at an angle of 120° and then these sliding regions grow (Figure 4.13(b)) and meet at the mid-thickness at 1650 μs. Upon further increase in the applied load, the sliding region widens in both +θ and -θ directions, as shown in Figure 4.13(c). At 5050 μs, an opening region initiates at an angle of 130°, at the middle of the sliding region (Figure 4.13(d)). When the applied load reaches its maximum value at 5550 μs, the opening region also reaches its widest boundaries which are between 94° and 180° and a relatively small sliding region remains at the top the opening between 71° and 94°, as shown in Figure 4.13(e).

As the unloading starts, the sliding region turns into sticking state; however, the opening region at the mating surfaces survives (Figure 4.13(f)). Upon unloading, the opening region starts to narrow (Figure 4.13(g)) rapidly and 850 μs after the start of unloading, the opening vanishes completely (Figure 4.13(h)). After the opening vanishes, a sliding region initiates at 94° as shown in Figure 4.13(i) and upon further unloading, the sliding region grows both in $+\theta$ and $-\theta$ directions and reaches its widest boundaries between 84° and 173° at the end of the cycle.

During the first 3000 μs of the loading of the 2nd cycle, the status of the lug and bush mating surfaces remains as sticking (Figure 4.13(k)). As the load increases, a sliding region initiates at an angle of 128° (Figure 4.13(l)) which lies uniformly in thickness-wise direction. Therefore, the slip fronts seen in Figure 4.13(l)-(o) are nearly flat, in contrast to curved slip fronts observed in the loading of the 1st cycle. After the initiation, the sliding region grows both in $+\theta$ and $-\theta$ directions upon further loading. At 4900 μs after the start of loading, mating lug and bush surfaces start to separate at 130°, as shown in Figure 4.13(m). The separation of mating surfaces was not observed in Al-Al lug-bush member; therefore, the mechanisms observed at the contact region of Al-steel lug-bush member differ from the mechanism of Al-Al lug-bush member mainly due to opening of the contact. As loading increases, the opening region starts to grow rapidly (Figure 4.13(n)) and reaches to its widest boundaries between 96° and 180° at the end of loading at 16650 μs. It is worth to note that the bottom of the lug and bush mating surfaces separate completely. At this point, a relatively small sliding region remains between 84° and 96°, at the top of opening region (Figure 4.13(o)).

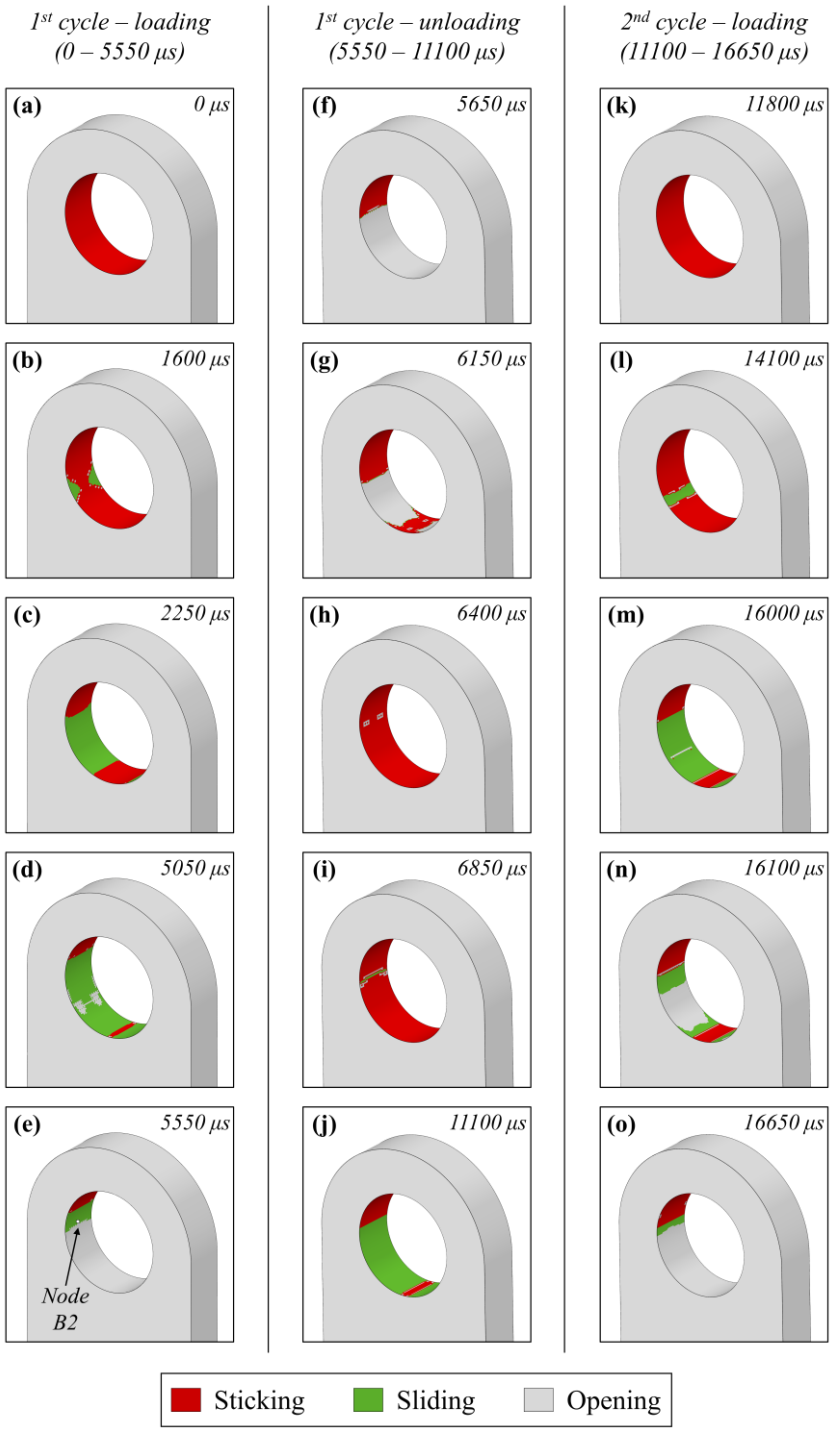


Figure 4.13. Evolution of sticking, sliding, and opening regions shown on the lug mating surfaces of Al-steel lug-bush member having a friction coefficient of 0.6 during (a)-(e) loading of the 1st cycle (0 – 5550 μs), (f)-(j) unloading of the 1st cycle, and (k)-(o) loading of the 2nd cycle. Sticking, sliding, and opening regions are represented with red, green, and grey, respectively.

Figure 4.14(a) shows the relative sliding distance of Node B1, which is located at the mid-thickness of the bush outer surface, with respect to its initially mating node, Node B2, which is located at the mid-thickness of lug inner surface (see Figure 4.13(e)) of Al-steel lug-bush member having a friction coefficient of 0.6. The Node B1 is selected at a location where the opening region does not reach throughout the cyclic loading. Figure 4.14(b) shows the rate of relative sliding of Node B1. The black dashed lines in both graphs show the times in which first sliding initiates at the contact region. The blue and orange dashed lines represent the times of opening initiation and disappearance, respectively.

Similar to the observations of Al-Al lug-bush member shown in Figure 4.5, slip rate of Node B1 increases rapidly when first sliding initiates at a location of the contact surface which is away from the location of Node B1. Until Node B1 starts to slide in the loading of the 1$^{st}$ cycle, it experiences elastic slip. Upon the reach of sliding region to Node B1, the slip rate continues to increase; however, with a decreasing slope. Even though the opening initiates at a location which is far from the Node B1, the almost-constant slip rate of this node starts to increase rapidly. At the end of the loading of the 1$^{st}$ cycle, the sign of the slip rate changes. During the elastic slip of Node B1, magnitude of the slip rate decreases until opening vanishes and sliding initiates. After the initiation of sliding at the contact region, slip rate becomes constant and it continues with the same constant value after Node B1 starts to slide. During the loading of the 2$^{nd}$ and the following cycles, slip rate does not reach the maximum value reached during the loading of the 1$^{st}$ cycle. Unloading of the following cycles exhibit the same behavior with the one of 1$^{st}$ cycle and Node B1 slides with respect to Node B2 approximately at a constant rate.

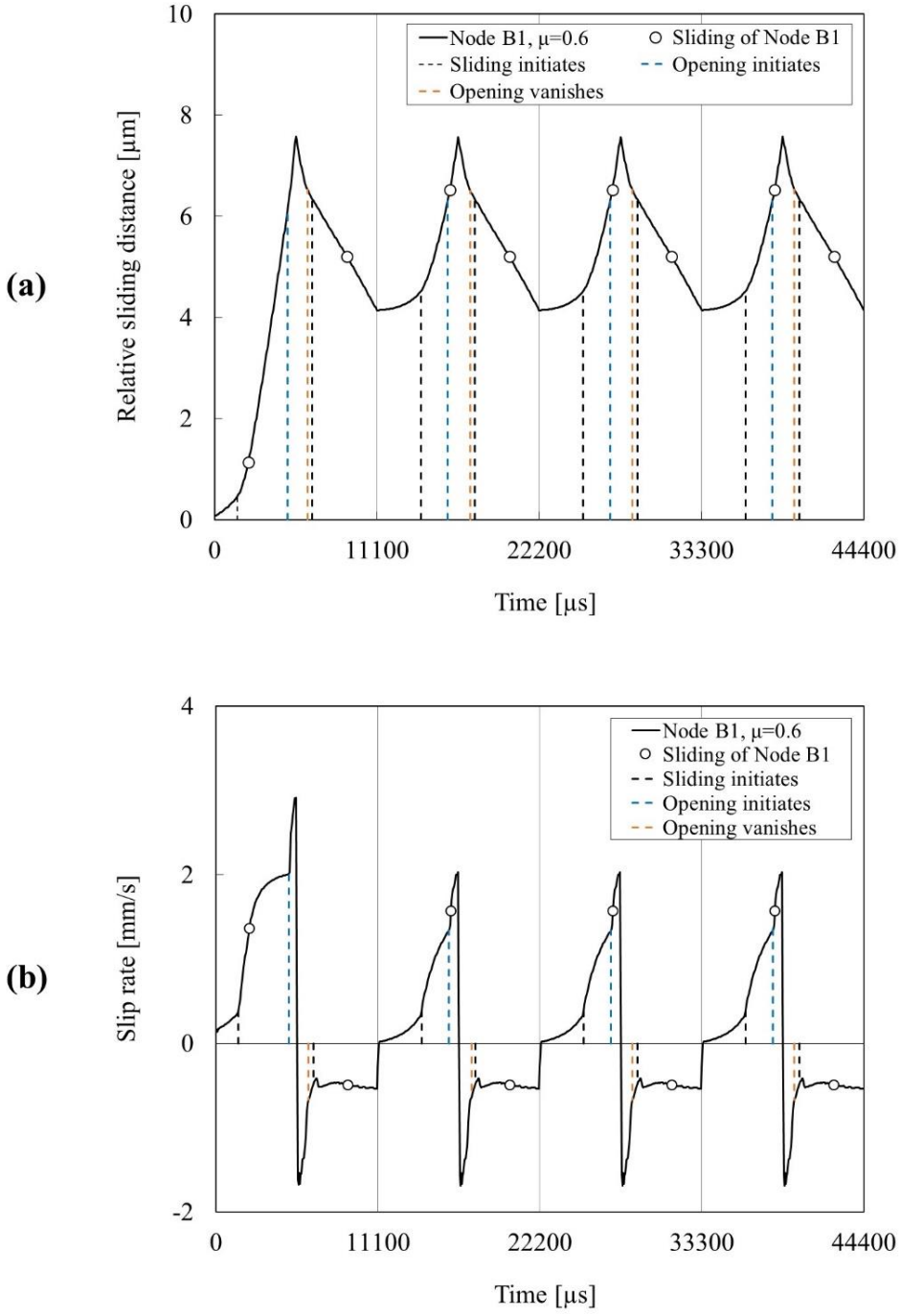


Figure 4.14. (a) Relative sliding distance and (b) slip rate of the Al-steel lug-bush member having a friction coefficient of 0.6 during four cycles. Black dashed lines show the times in which the first sliding at the contact area initiates. The circular markers indicate the times in which sliding of Node B1 initiates. Blue and orange dashed lines represent the times in which opening at the contact region initiates and vanishes, respectively.

The comparison of critical shear stress values and shear stresses at the mating lug surface is conducted along a path in Al-steel lug-bush member in order to learn whether the sticking regions around the sliding region have very close shear stress values to the critical shear stresses. Figure 4.15 shows the present and critical shear stress distributions with black and red dashed lines, respectively, at the end of loading of the 2nd cycle. Both shear stresses are equal to zero after 90° since these regions are separated at the end of loading. Similar to the Al-Al lug-bush case, there is a minute difference between the critical and present shear stresses in the sliding regions approximately between 70° and 85°.

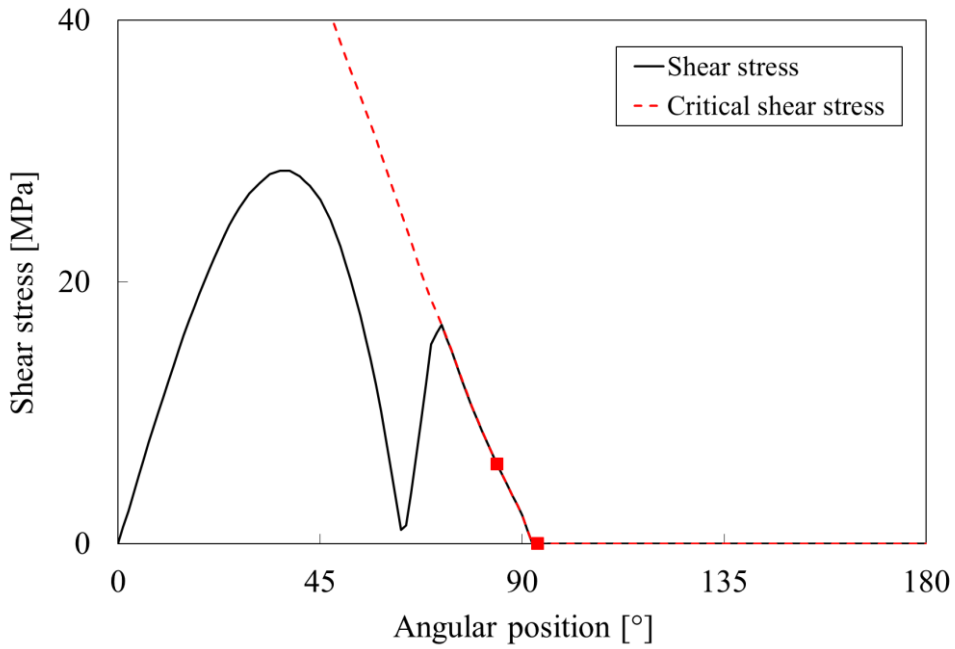


Figure 4.15. Resultant shear stress vs. angular position graph showing the shear stress and critical shear stress distributions at the end of loading of the 2nd cycle. Shear stress data are taken along a path at the mid-thickness of the lug mating surface of Al-steel lug-bush member having a friction coefficient of 0.6. The left and right square markers indicate the upper and lower boundaries of the sliding region. The region having zero shear stress corresponds to the opening region.

Since the shear stress distributions are approximately equal at the sticking regions, the model of this specimen is modified in a similar way to what is performed in Al-Al lug-bush member case such that the loading continues during additional 600 μs

after it reaches its previous maximum value at 16650 μs. Results of the modified simulation show that as the load is increased beyond its previous maximum value, the sticking regions start to slide immediately, as shown in Figure 4.16. A sliding region initiates at approximately 70° and propagates towards the existing sliding region (Figure 4.16(b)-(c)). The sliding region grows and unites with the existing one within 1 μs (Figure 4.16(d)) creating a united sliding region which lies between 71° and 94°. While the lower front of the newly developed sliding region propagates towards the existing one, the lower front travels 1.03 mm in 0.2 μs, as shown in Figure 4.16(b) and (c). The average speed of the lower front is calculated as 5150 m/s. The extent of the sliding region does not change under further loading.

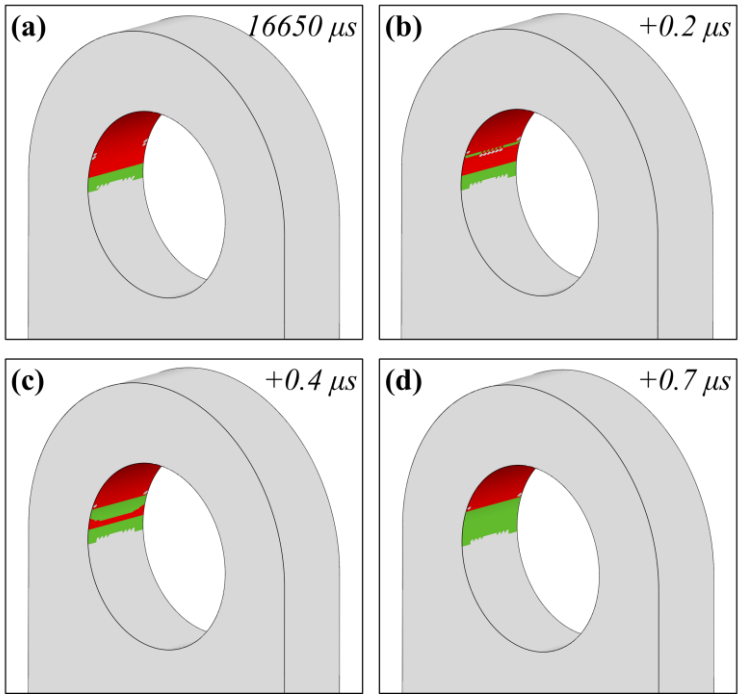


Figure 4.16. Evolution of newly developed sliding regions in the case of continuing applied load after it reaches its previous maximum value at 16650 μs in Al-steel lug-bush member having a friction coefficient of 0.6. Dynamic evolution of the sliding regions is shown (a) at 16650 μs, which is the state reached at the previous maximum load, and after (b) 0.2 μs, (c) 0.4 μs, and (d) 0.7 μs.

Figure 4.17(a) shows the location of sliding nodes during the 4 cycles in Al-steel lug-bush member having a friction coefficient of 0.6. Each sliding is shown with a black dot and the red and blue lines represent the location of upper and lower slip fronts throughout the loading. At the ends of loading, sliding and opening regions exist together and the opening at these points can be seen as blank regions below the sliding regions in Figure 4.17(a). During the unloading, upper slip front does not propagate as much as the lower slip front. Figure 4.17(b) shows the difference between the distances covered by upper and lower slip fronts during unloading. Hence, the speed of lower slip front during unloading is greater than the speed of loading. Similar to the Al-Al lug-bush member case, speed values decrease up to 0 m/s at the ends on one-half cycles. Since the slip fronts are not propagating continuously, the speed distribution is not smooth.

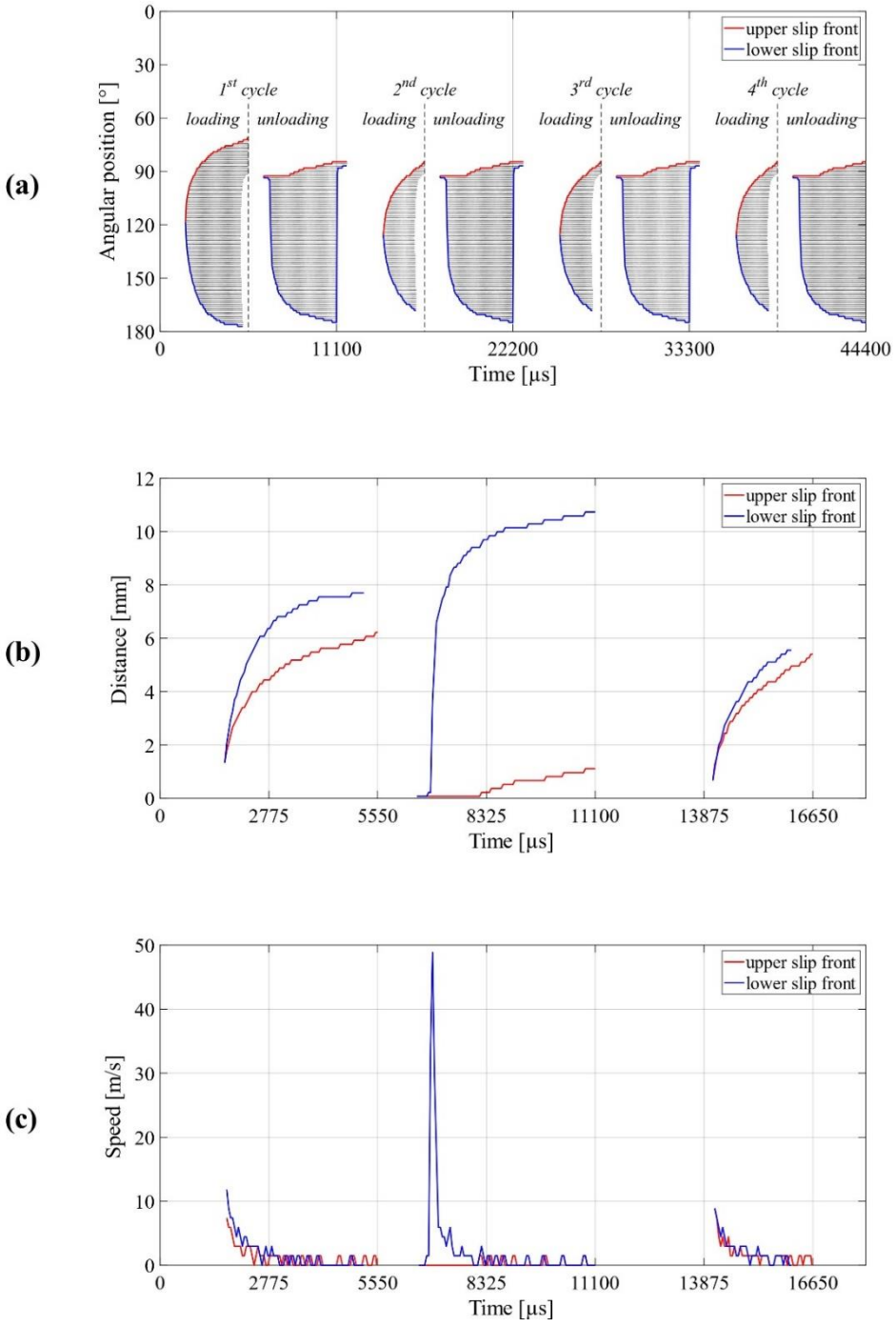


Figure 4.17. (a) Angular position vs. time graph of the sliding nodes which are represented with black dots throughout the four cycles of Al-steel lug-bush member having a friction coefficient of 0.6. The upper and lower slip fronts are shown with red and blue curves. (b) Distance and (c) speed curves of the upper and lower slip fronts with respect to time during the loading and unloading of the 1st cycle and loading of the 2nd cycle.

The maximum sliding region areas reached during the loading of the 1st and 2nd cycles and unloading of the 1st cycle when the friction coefficient is taken as $\mu = 0.6$ and $\mu = 0.8$ are summarized in Figure 4.18(a). Similar to Al-Al lug-bush member, the maximum sliding region reached during the loading of the 1st cycle is greater than that of following half-cycles. However, in contrary to Al-Al case, the extent and location of maximum sliding regions are not the same during the steady state loading and unloading responses. At the end of loading of the 2nd and the following cycles, if the same applied load is continued instead of unloading, a new sliding region initiates at 71°. This newly developed sliding region propagates towards the existing one and unites with it in just 0.5 μs. The sliding region distributions at these points are also shown in Figure 4.18(a). However, when dynamic propagation of the sliding region occurs in the case of continuing applied load, opening region exists at the surface and the extent of the resultant sliding region is still smaller than the maximum extent reached during the loading, which occurs prior to opening initiation. The distribution of the sliding regions when friction coefficient is increased to 0.8 from 0.6 is also shown. Similar to the observations of Al-Al lug-bush member, extent of the sliding regions decrease as the friction coefficient increases.

The locations of tribolayer regions observed in the tested Al-steel lug-bush member are presented in Figure 4.18(b). The RHS and LHS of the specimen does not have the same tribolayer distributions. However, both tribolayer regions are continuous in contrast to Al-Al specimen. The extent of the tribolayer regions is smaller when compared to maximum sliding regions obtained in the simulations when as $\mu = 0.6$ and $\mu = 0.8$.

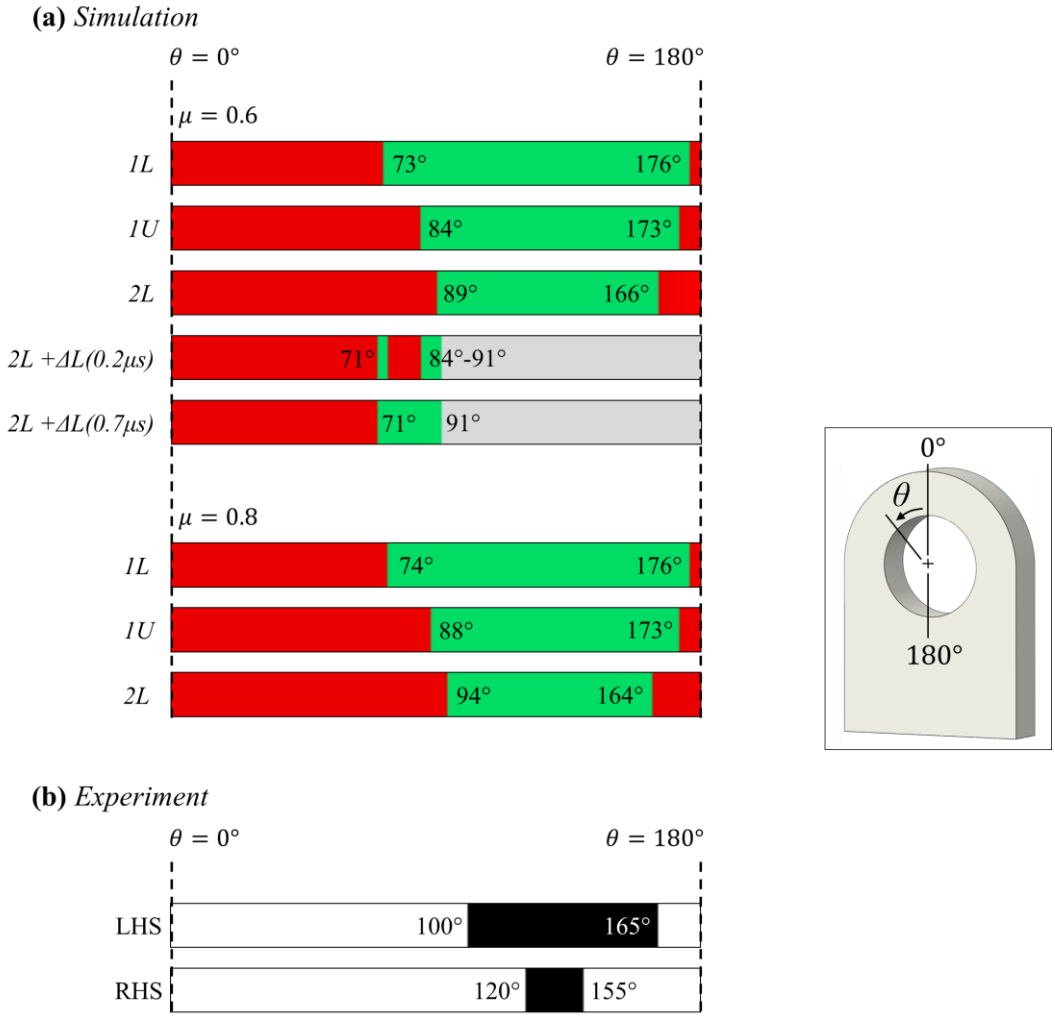


Figure 4.18. Locations of the maximum sliding regions on the lug mating surface during loading of the 1st cycle (1L), unloading of the 1st cycle (1U), and loading of the 2nd cycle (2L) of Al-steel lug-bush member at two different friction coefficients (0.6 and 0.8). The sliding regions obtained by increasing the maximum load incrementally for the friction coefficient of 0.6 are also shown (2L+ΔL). Sticking, sliding, and opening regions are represented with red, green, and grey, respectively. (b) Locations of the tribolayer regions observed on both LHS and RHS of the bush mating surface of tested Al-steel lug-bush member in which black represents the regions with tribolayer and white represents the clean regions.

## 4.3 Investigation of Ti-Steel lug-bush member

The numerical results of the cyclic loading of Ti lug and steel bush specimen having a stress ratio of 0.1 are presented in this section. Simulations are carried out using two different friction coefficient values which are 0.6 and 0.8 in order to investigate the effect of friction coefficient.

Figure 4.19 shows the applied load vs. time graph of the Al-steel lug-bush member. The letters on the applied load graph shows the corresponding load and time values of the sticking-sliding states shown in Figure 4.21 during the loading of the 1st and 2nd cycles and unloading of the 1st cycle.

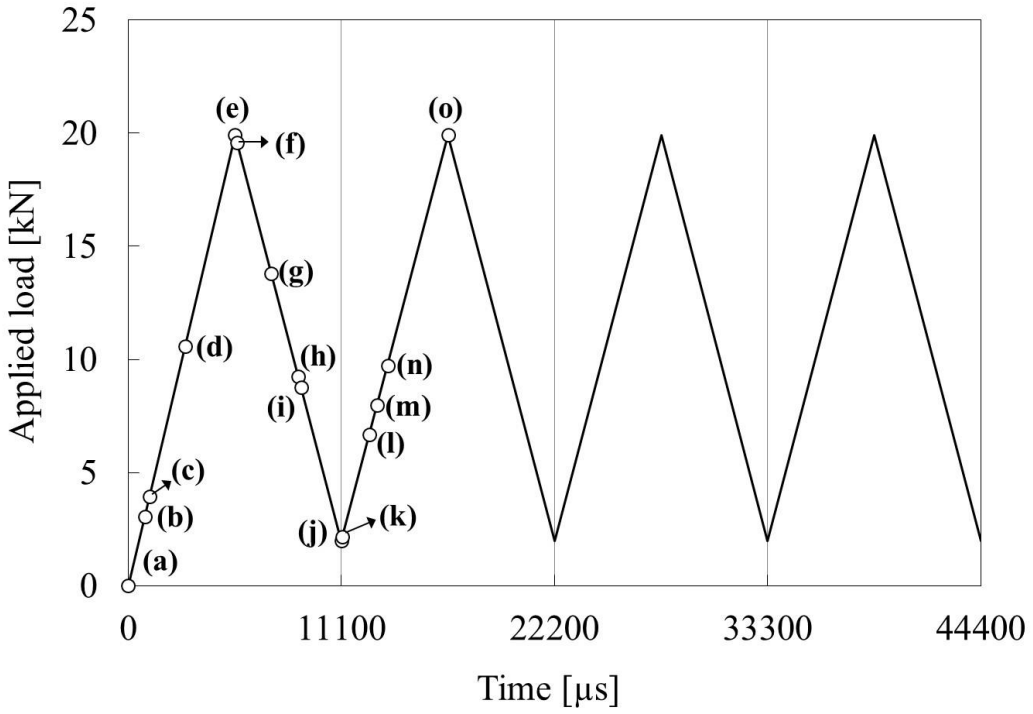


Figure 4.19. Applied load vs. time graph of Ti-Steel lug-bush member. The load is applied to the bush inner surface as pressure in cosine form, where the maximum applied pressure of 306 MPa corresponds to a maximum applied load of 19921 N. The letters show the time and load values of sticking-sliding states shown in

Figure 4.20 shows the general load-displacement behavior of Ti-steel lug-bush member during 4 cycles when the friction coefficient is 0.6. Similar to the behavior

observed in Al-Al and Al-steel lug-bush members, the loading of the 1st cycle is not identical with the loading of the following cycles. The remaining loading and unloading curves of the following cycles are approximately identical. This behavior shows that the earliest steady state response is reached during the 2nd cycle. The steady state behavior is also observed in the relative sliding vs. time graphs which will be discussed in this section. Therefore, the sliding evolution at the lug mating surface is presented during the loading and unloading of the 1st cycle and loading of the 2nd cycle in Figure 4.21 for simplicity reasons since the steady state response repeats in the following cycles.

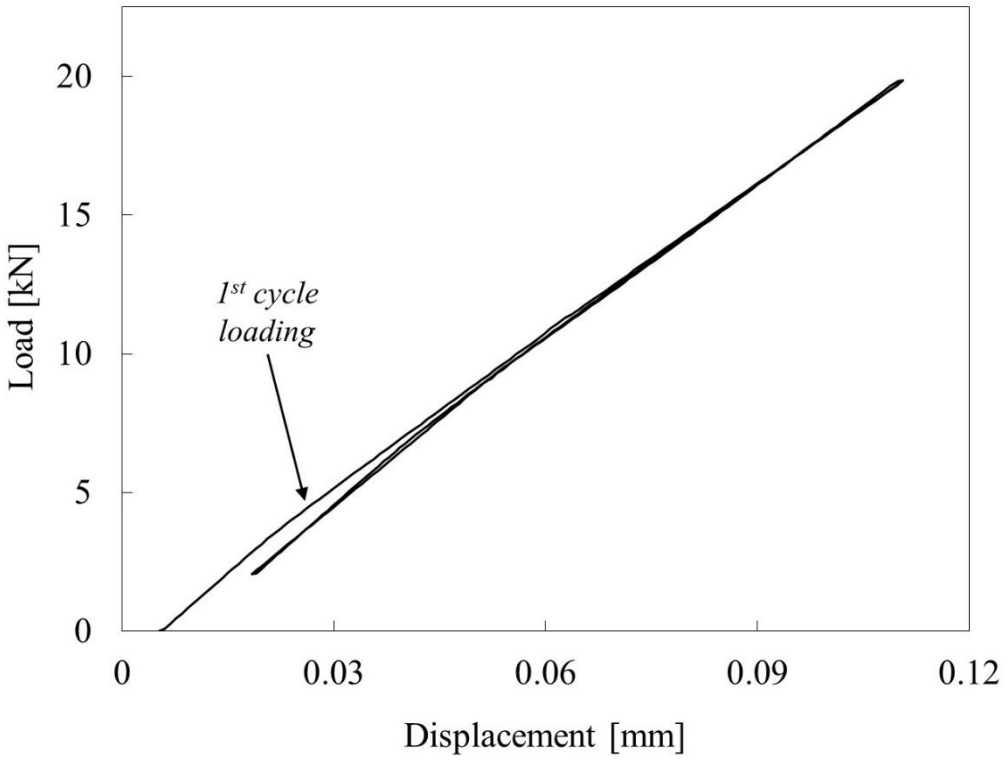


Figure 4.20. The load vs. displacement graph of the Ti-steel lug-bush member having a friction coefficient of 0.6. The displacement data is obtained at a node resting at the edge of inner lug surface where $\theta = 0°$.

The sticking, sliding, and opening states of the lug mating surface when the friction coefficient is equal to 0.6 are shown in Figure 4.21(a)-(e) during the loading of the 1st cycle, in Figure 4.21(f)-(j) during the unloading of the 1st cycle, and in Figure

4.21(k)-(o) during the loading of the 2nd cycle. Throughout the evolutions shown in Figure 4.21, only the left-hand-side of the lug mating surface is shown since the sticking and sliding states are identical at the right- and left-hand sides of the lug and bush.

The sliding evolution of the Ti-steel lug-bush member is very similar to the evolution observed in Al-steel lug-bush member. The initiation and propagation of the sliding region, and initiation of opening during the loading of the 1st cycle happens with the same sequence when compared with the Al-steel case. First sliding initiates at an angle of 119° at 850 μs at the edges of the lug mating surface (Figure 4.21(b)). As the applied load increases, sliding regions meet at the mid-thickness at 900 μs and propagate along both +θ and -θ directions (Figure 4.21(c)). Upon further loading, an opening region initiates at 130° in the middle of the sliding region at 2900 μs. This opening region grows rapidly and reaches the state shown in Figure 4.21(d) in 50 μs. As the applied load increases further, the opening region grows and covers the bottom of the mating surface; however, the sliding region still exists at the top of the opening. When the loading reaches its maximum value of 306 MPa, the boundaries of the sliding and opening regions are at 64°-87° and 87°-180°.

As soon as unloading starts, the sliding region disappears similar to the observations of Al-Al and Al-steel cases. As the applied load decreases, upper front of the opening region starts to recede. As the upper front of opening region recedes, a sliding region initiates at the upper front of the opening, between the opening and sticking regions. Upon further unloading, the sliding region grows, and the opening region continues to recede together. However, at some point, the upper front of the opening region recedes rapidly than the propagation of lower slip front, leaving a sticking region between the sliding and opening as shown in Figure 4.21(h). Then, the opening region narrows rapidly and vanishes at 9000 μs (Figure 4.21(i)). At 250 μs after the opening disappears, the sliding region starts to grow rapidly in +θ direction. The sliding region reaches its widest boundaries between 72° and 173° at the end of unloading at 11100 μs (Figure 4.21(j)) by propagating only its lower front. The unloading half cycles of Ti-steel case differs from the unloading of Al-steel case. In

the Al-steel case, the opening vanishes first, and a sliding region initiates afterwards. However, in Ti-steel case, the sliding initiates before the opening region disappears.

As soon as loading of the 2nd cycle starts, most of the sliding region vanishes; however, a small sliding region remains (Figure 4.21(k)) and narrows slowly upon loading. At 12550 μs, a new sliding region initiates at 126° just before the previous sliding region vanishes as shown in Figure 4.21(l). Upon further loading, the sliding region grows in both +θ and -θ directions (Figure 4.21(m)). Similar to the loading of the 1st cycle, an opening region initiates at the middle of the sliding at 130° as the applied load increases further. When the applied load reaches its maximum value of 306 MPa at 16650 μs, the boundaries of the sliding and opening regions are at 65°-87° and 87°-180°.

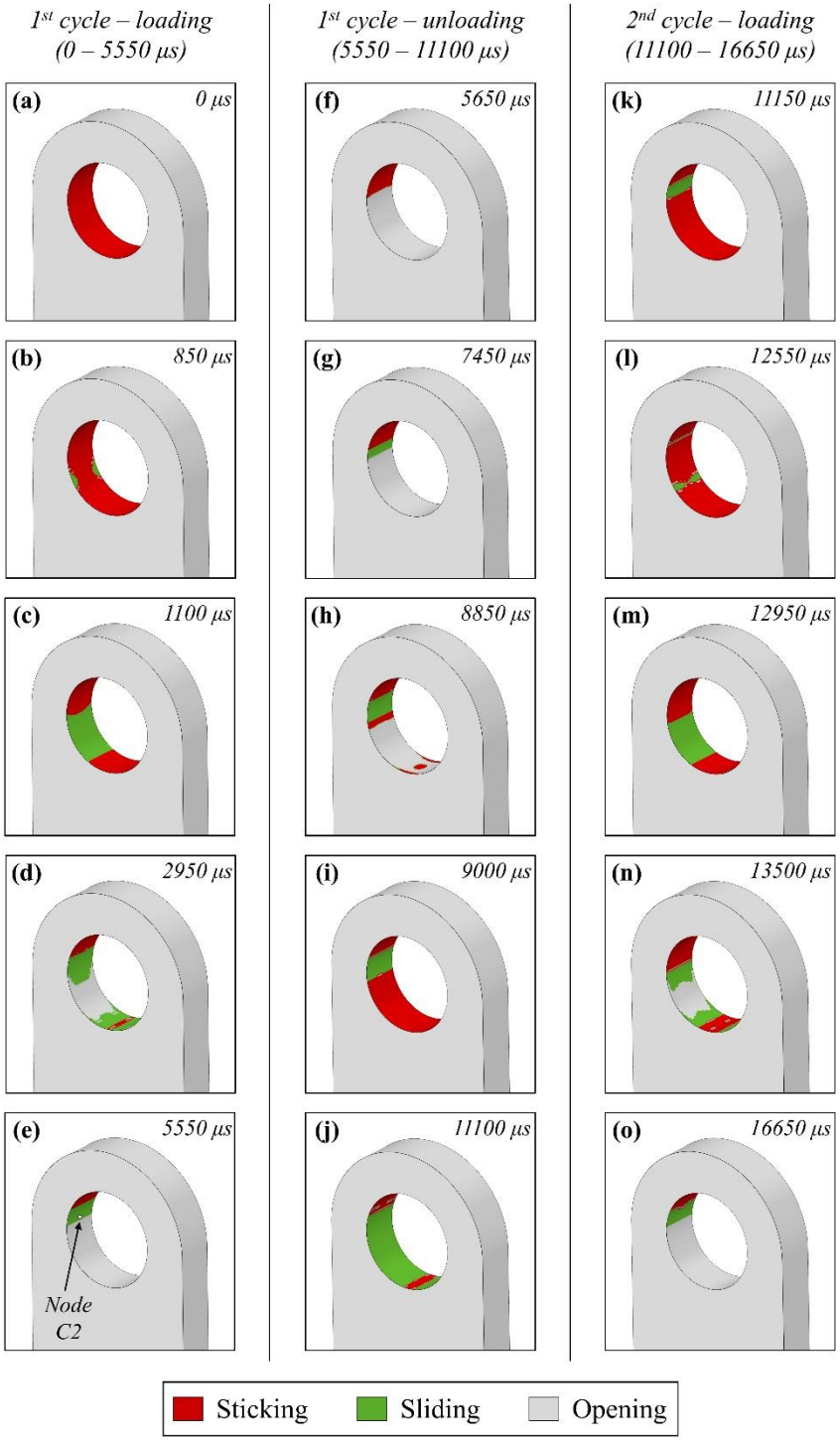


Figure 4.21. Evolution of sticking, sliding, and opening regions shown on the lug mating surfaces of Ti-steel lug-bush member having a friction coefficient of 0.6 during (a)-(e) loading of the 1st cycle (0 – 5550 μs), (f)-(j) unloading of the 1st cycle, and (k)-(o) loading of the 2nd cycle. Sticking, sliding, and opening regions are represented with red, green, and grey, respectively.

Figure 4.22(a) shows the relative sliding distance of Node C1, which is located at the mid-thickness of the bush outer surface, with respect to its initially mating node, Node C2, which is located at the mid-thickness of lug inner surface (see Figure 4.21(e)) of Al-steel lug-bush member having a friction coefficient of 0.6. Node C2 is resting at the upper parts of the lug mating surface where the opening does not reach throughout the four cycles. The black dashed lines in below graphs show the times in which first sliding initiates at the contact region while the blue and orange dashed lines represent the times of opening initiation and disappearance, respectively.

Figure 4.22(b) shows the slip rate of Node C1 during four cycles. The slip rate of this particular node is affected by the opening of this node which is shown with circular markers. When the opening and sliding initiates or opening vanishes at a distant location, the relative sliding distance and the slip rate of Node C1 changes even though these evolutions are occurring away from that node. During the loading of all cycles, slip rate starts to increase rapidly upon initiation of first sliding or first opening at the contact region. After the rapid increase in slip rate due to abovementioned events, slip rate continues to increase with a decreasing rate; however, it cannot reach a constant slip rate value. In the unloading of all four cycles, slip rate reaches a constant value after the opening vanishes towards the end of these one-half cycles.

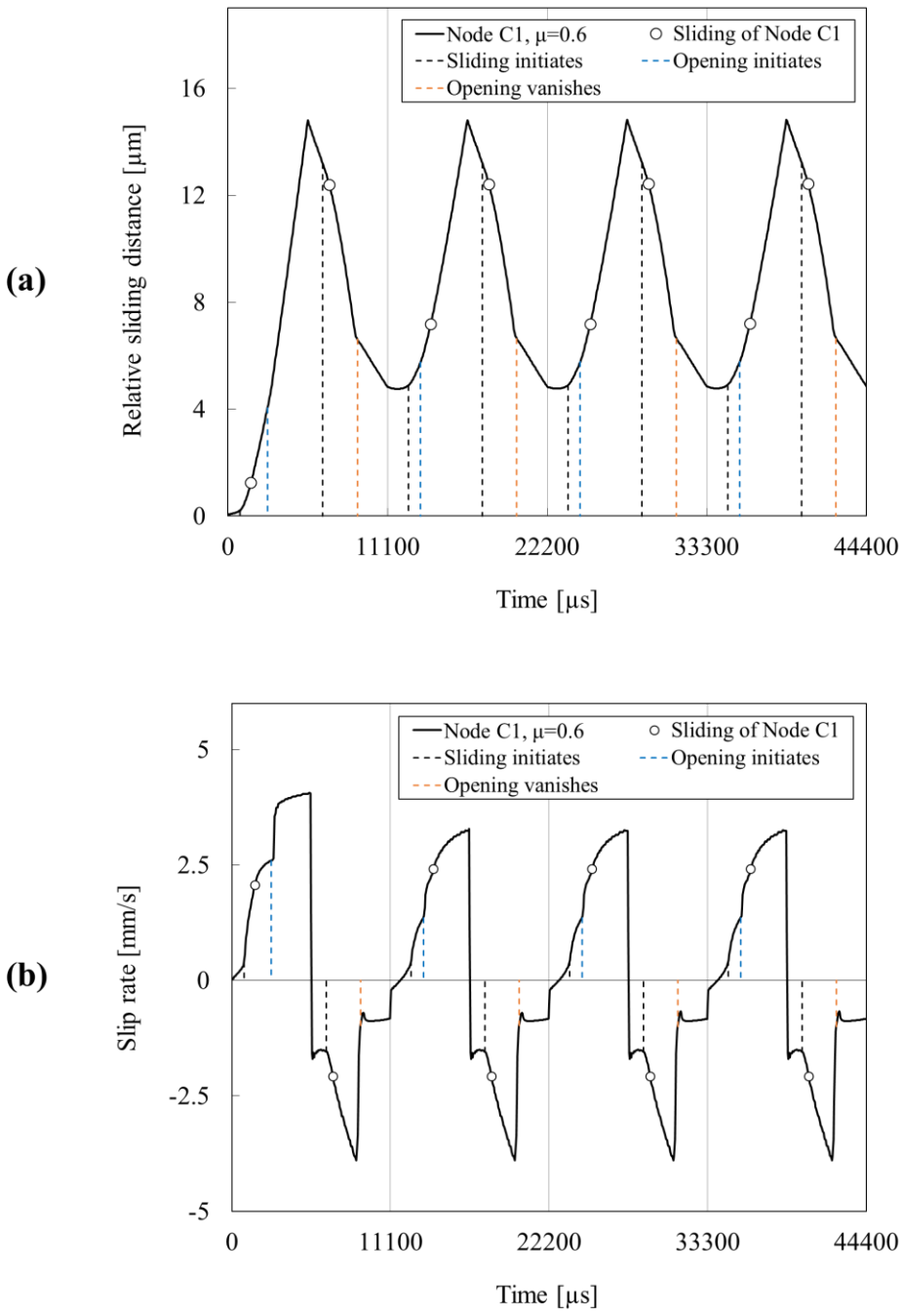


Figure 4.22. (a) Relative sliding distance and (b) slip rate of the Ti-steel lug-bush member during four cycles with a friction coefficient is 0.6. Black dashed lines show the times in which the first sliding at the contact area initiates. The circular markers indicate the times in which sliding of Node C1 initiates. Blue and orange dashed lines represent the times in which opening at the contact region initiates and disappears, respectively.

Figure 4.23(a) shows the location of sliding nodes during the 4 cycles in Ti-steel lug-bush member having a friction coefficient of 0.6. Each sliding is shown with a black dot and the red and blue lines represent the location of upper and lower slip fronts throughout the loading. Opening initiates at the ends of loading half cycles and vanishes during the unloading half cycles, after the sliding is initiated. The opening regions can be seen as blank regions below the sliding regions in Figure 4.23(a). Similar to the previous cases, lower slip fronts cover greater distances in all half cycles and therefore they reach greater speed values. Since the lower slip front propagates rapidly after the opening vanishes during unloading, it reaches higher values, 40 m/s at the beginning, when compared with the slip front values reached during loading. Since the slip fronts are not propagating continuously, the speed distribution is not smooth.

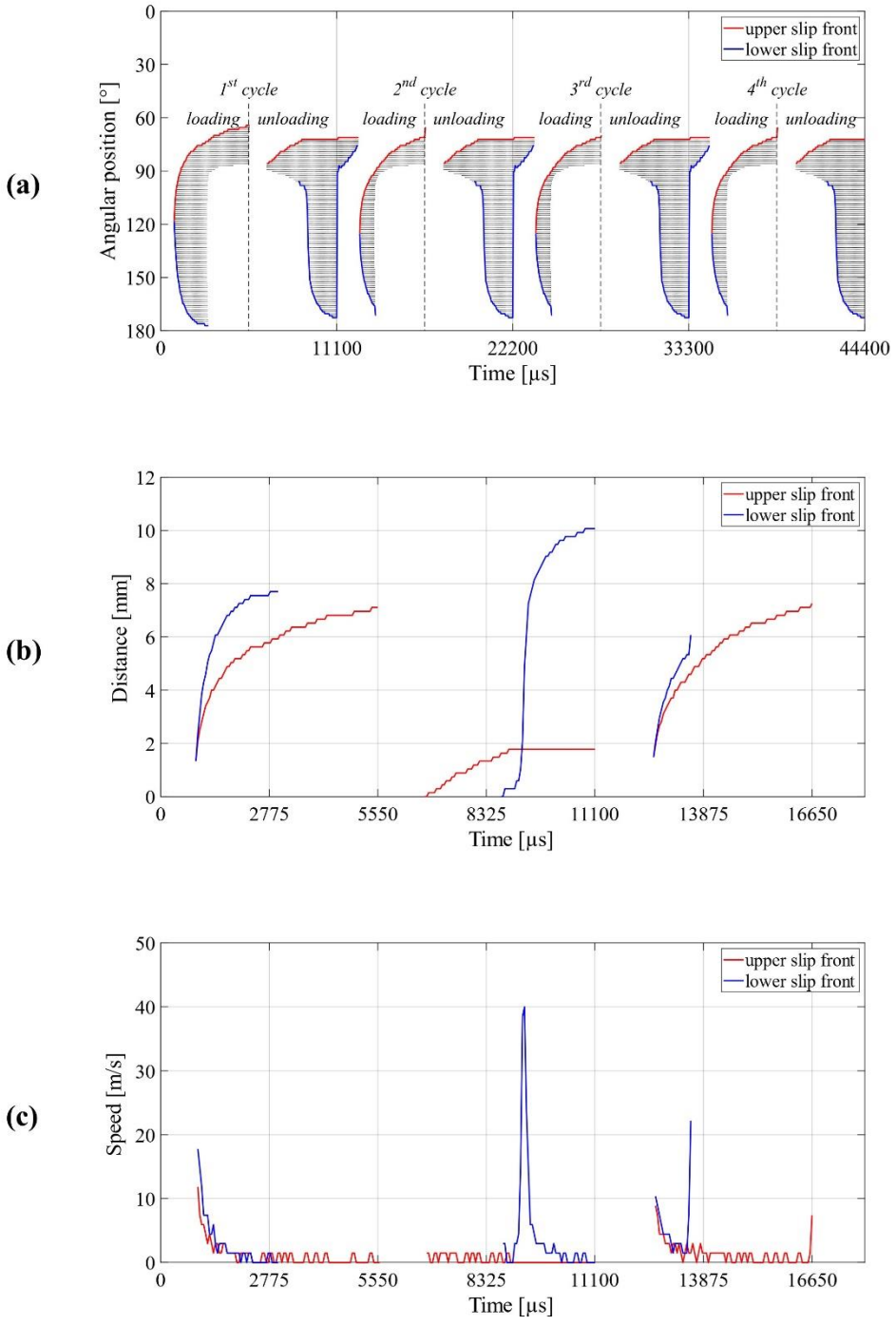


Figure 4.23. (a) Angular position vs. time graph of the sliding nodes which are represented with black dots throughout the four cycles of Ti-steel lug-bush member having a friction coefficient of 0.6. The upper and lower slip fronts are shown with red and blue curves. (b) Distance and (c) speed curves of the upper and lower slip fronts with respect to time during the loading and unloading of the 1st cycle and loading of the 2nd cycle.

The maximum sliding areas in Ti-steel lug-bush member reached during the loading of the 1st and 2nd cycles and unloading of the 1st cycle when the friction coefficient is taken as $\mu = 0.6$ and $\mu = 0.8$ are summarized in Figure 4.24(a). As the friction coefficient increases from 0.6 to 0.8, the maximum sliding areas decrease; however, the small decrease however, the location of lower sliding front remains the same, approximately, during the unloading of the 1st cycle. The decrease in the sliding region areas during the unloading of the 1st cycle happens mainly by the retraction of upper sliding fronts. Figure 4.24(b) shows the experimental observations of the tribolayer locations in both Ti-steel specimens. The first specimen displays nearly identical tribolayer regions at the LHS and RHS with a discontinuous distribution. On the other hand, the second specimen has different tribolayer areas and locations at the LHS and RHS of the specimen with a continuous tribolayer distribution. The numerical results exhibit similar lower sliding region boundaries during the loading of the 2nd cycle when compared to the lower tribolayer locations of the tested specimens. However, sliding regions reached during the unloading cycles has greater extent and does not display similar results. Increasing the friction coefficient value would decrease the sliding region areas; therefore, the boundaries of the sliding regions with a higher coefficient of friction would obtain better correlation with the tribolayer locations.

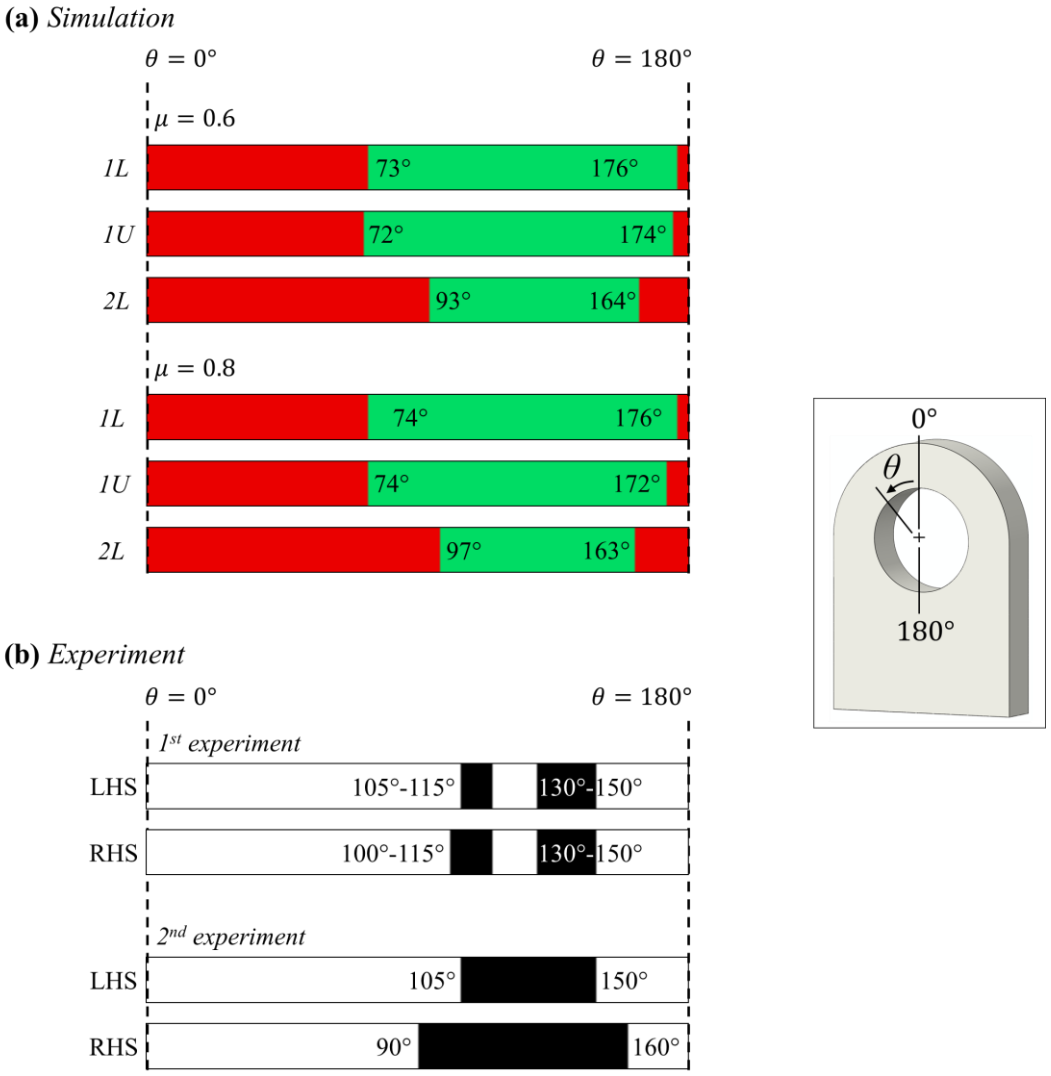


Figure 4.24. (a) Locations of the maximum sliding regions on the lug mating surface during loading of the 1st cycle (1L), unloading of the 1st cycle (1U), and loading of the 2nd cycle (2L) of Ti-steel lug-bush member at two different friction coefficients of 0.6 and 0.8. The sliding regions obtained by increasing the maximum load incrementally for the friction coefficient of 0.6 is also shown (2L+ΔL). Sticking, sliding, and opening regions are represented with red, green, and grey, respectively. (b) Locations of the tribolayer observed on both LHS and RHS of the bush mating surface of two tested Ti-steel lug-bush members in which black represents the regions with tribolayer and grey represents the clean regions.

## 4.4 Prediction of crack initiation locations

In this section, the results obtained from the prediction of fretting crack initiation locations using two different stress-strain based multiaxial fatigue damage criteria, namely Fatemi-Socie and Smith-Watson-Topper, will be presented. These criteria calculate the damage parameter at all points of the contact region using the stress and strain distributions and predict the crack initiation location as the point where the damage parameter is maximized. In our case, the stress and strain distributions are obtained at the lug mating surface for Al-Al, Al-steel, and Ti-steel lug-bush members having friction coefficients of 1, 0.6, and 0.6, respectively. The results of the simulations are compared with the experimental evidence in terms of crack locations.

In order to predict the crack initiation locations of all members, the stresses and strains are obtained from the results of the FEA along a path taken at the mid-thickness of the lug during the loading of the $1^{st}$ and $2^{nd}$ cycles. Since the earliest steady-state response is reached during the $2^{nd}$, it is of importance whether the damage parameters predict different crack initiation locations if the loading of the $1^{st}$ cycle is considered.

Figure 4.25 shows the FS and SWT damage parameter distributions of Al-Al, Al-steel, and Ti-steel lug-bush members having friction coefficients of 1, 0.6, and 0.6, respectively. The distributions are calculated using the stress and strain distributions along a path at the mid-thickness of the lug mating surface. The FS and SWT parameter distributions are shown with black and red lines, respectively; whereas the distributions at the loading of the $1^{st}$ and $2^{nd}$ cycles are shown with solid and dashed lines, respectively.

For the Al-Al member, the predicted crack locations lie between 82° and 86°. FS predicts the crack locations as 86° and 82° for the $1^{st}$ and $2^{nd}$ cycles, respectively, while SWT predicts as 86° and 84° for the $1^{st}$ and $2^{nd}$ cycles, respectively (Figure 4.25(a)).

For the Al-steel member, the predicted crack location is 90° by both FS and SWT when the 2nd cycle is considered. If the 1st cycle is considered, the predicted crack initiation locations are found as 87° by both FS and SWT (Figure 4.25(b)).

For the Ti-steel lug-bush member shown in Figure 4.25(c), the predicted crack locations by FS and SWT are 85° and 86°, respectively, when 1st cycle is considered. FS and SWT parameters predict the crack location as 85° and 86° if the 2nd cycle is considered.

It can be observed that the predicted crack locations are close to each other for the 1st and 2nd cycles with both FS and SWT damage criteria. However, the crack locations observed in the tested specimens are 105° for two Ti-steel specimens, 100° for Al-Al specimen, and 100°&120° for Al-steel specimen. The predicted crack locations by the FS and SWT deviate from the observed crack locations by minimum of 10°.

Figure 4.26 shows the comparison of the FS and SWT damage parameters along two paths located at the edge and mid-thickness of the lug mating surface. The predicted crack locations calculated at the edge and mid paths for Al-Al lug-bush member are 80° and 81° when FS is used and 83° and 84° when SWT is used. The results of Al-Steel and Ti-Steel lug-bush members predict the same locations for both edge and mid paths as 88°&90° and 84°&86° with FS and SWT, respectively. The edge effect seen in the evolution of sliding regions has no effect on the predicted crack locations.

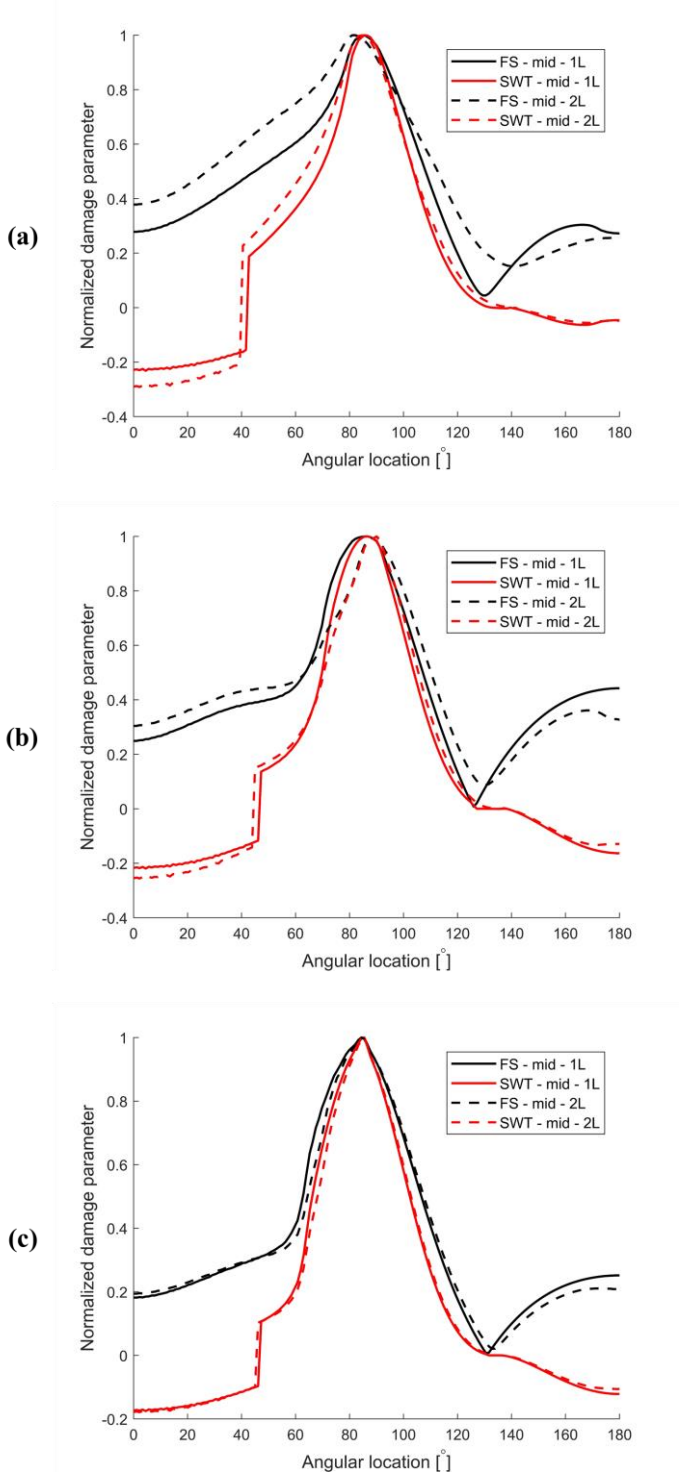


Figure 4.25. Comparison of FS and SWT parameter distributions along a path taken at the mid-thickness of the lug mating surface during the loading of 1st and 2nd cycles of (a) Al-Al, (b) Al-steel, and (c) Ti-steel lug-bush members having friction coefficients of 1, 0.6, and 0.6, respectively.

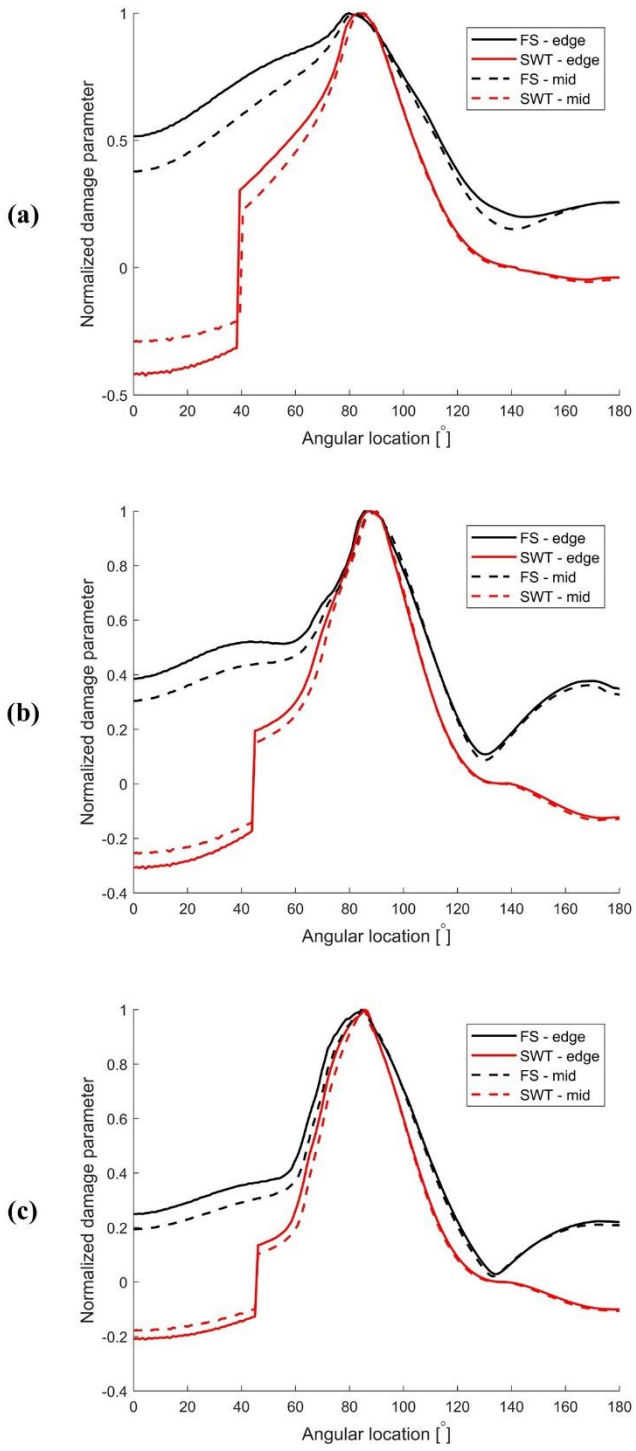


Figure 4.26. Comparison of FS and SWT parameter distributions along mid and edge paths taken at the edge and mid-thickness of the lug mating surface during the loading of the 2nd cycle of (a) Al-Al, (b) Al-steel, and (c) Ti-steel lug-bush members having friction coefficients of 1, 0.6, and 0.6, respectively.

# CHAPTER 5

# CONCLUSION

In this study, experimental and numerical investigations of lug-bush members under cyclic loading are presented. Four lug-bush members, which are Al lug – Al bush member, Al lug – steel bush member, and two Ti lug -steel bush members, were tested under fatigue loading conditions where the stress ratio is 0.1 and the frequency is 90 Hz. Failure occurred in the lugs due to a crack initiated at the contact region. Post-mortem experimental investigations of the lug-bush members are conducted with digital microscope and SEM. Detailed macroscopic and microscopic investigations of mating surfaces revealed that:

- Mating surfaces worn out due to relative motion. The worn metallic particles oxidize and create tribolayer regions, which are observed as black-brown residues on the mating lug and bush surfaces of tested specimens.
- The content of the tribolayer regions is examined with Energy Dispersive Spectroscopy analysis using SEM. Results showed that the tribolayer regions include considerable amount of oxygen (20% by mass) whereas the clean regions have no oxygen content. Therefore, the regions where tribolayer exists are found to be sliding regions.
- Microscopic investigations of these sliding regions show that there exists a sharp boundary between the tribolayer and clean regions.
- Maps of sliding regions and crack locations are generated for all tested specimens. The crack locations are observed to be consistently in the vicinity of sliding region boundaries for all specimens.
- The tribolayer regions at the RHS and the LHS of the bush outer surface are not the same. The unsymmetrical distribution of tribolayer regions may be due to possible imperfections of the experiments.

- Discontinuous tribolayer regions are observed at the contact regions of Al-Al specimen and one of Ti-steel specimens. The other Ti-steel specimen and the Al-steel specimen have continuous tribolayer distributions.
- The tribolayer shapes are observed to be different in Al-Al case when compared to Al-steel and Ti-steel specimens. Rounded tribolayer regions are observed at the lug inner and bush outer surfaces of Al-Al specimen whereas the tribolayer regions of Al-steel and Ti-steel specimens are directional and discontinuous in the thickness-wise direction.

Numerical investigations of the lug-bush members are conducted using a commercial finite element program (ABAQUS) and the experimental conditions are simulated for all specimens on a 3-D model with implicit-dynamic analysis method. Interference fit of the bush into the lug is performed and 4 cycles are simulated. A distributed pressure having a stress ratio of 0.1 is applied to the upper half of the bush inner surface in cosine distribution in order to represent the pin loading applied during the experiments. Contact is defined between the lug inner surface and bush outer surface where the tangential behavior is modeled with Coulomb law using penalty approach. Static coefficient of friction values are defined for each material combination and the effect of change in the friction coefficient on sliding region areas is observed. The numerical results show that:

- When cyclic loading is applied, the response during the cycles is found to reach a steady-state in the $2^{nd}$ cycle when load-displacement behavior, evolution of sliding regions, and relative sliding distances of each cycle are compared. Therefore, it is important to simulate cyclic loading if the fatigue loading is investigated. Evaluation of fatigue damage parameters using the results of a cycle which did not reach the steady state would result in misleading crack initiation locations and lives.
- The evolution sliding regions are obtained for each material combination. In Al-Al lug-bush member, sliding and sticking regions are observed throughout the cyclic loading. The greatest sliding regions during loading and

unloading are reached at the ends of each one-half cycle. As the half cycle ends, sliding regions disappear and turn into sticking region. In Al-steel and Ti-steel lug-bush members, opening regions are observed in addition to sticking and sliding regions. These opening regions initiate during the loading, continue to exist as the half cycle is ended, and disappear rapidly during the unloading. In Ti-steel lug-bush member, a portion of sliding regions do not disappear as soon as the unloading ends and loading starts, in contrary to other material combinations.

- Increase in the friction coefficient decreases the extent of sliding regions.
- Relative sliding displacement and slip rate of a node experiences sharp changes when sliding and opening initiates or opening disappears even though these changes occur at distant locations.
- Sliding regions occurring during the loading of the $2^{nd}$ cycle are observed to be smaller than that of loading of the $1^{st}$ cycles. An infinitesimal increase in the load after reaching its maximum value results in initiation of new sliding regions and dynamic propagation of these newly developed slip fronts. In other words, if a small disturbance is applied to the maximum loading value, a different sliding mechanism occurs which includes dynamic propagation of slip fronts.
- The reason for discontinuous sliding regions observed in the experiments may be due to small disturbances to the maximum load value during the experiments.
- FS and SWT damage parameters are observed to be incapable to predict the crack initiation locations in this problem. Predicted crack locations are not the same when the stress values of the $1^{st}$ and $2^{nd}$ cycles are used.
- Boundaries of the sticking and sliding regions obtained from the simulations are consistent with the experimental observation of crack initiation locations.

## REFERENCES


[1] Eden, E. M., Rose, W. N., & Cunningham, P. L. (1911). The endurance of metals: experiments on rotating beams at University College, London. *Proceedings of the Institution of Mechanical Engineers*, *81*(1), 839-974.

[2] Vadiraj, A., & Kamaraj, M. (2007). Effect of surface treatments on fretting fatigue damage of biomedical titanium alloys. *Tribology International*, *40*(1), 82-88.

[3] O'Halloran, S. M., Connaire, A. D., Harte, A. M., & Leen, S. B. (2016). Modelling of fretting in the pressure armour layer of flexible marine risers. *Tribology International*, *100*, 306-316.

[4] Wang, D., Zhang, D., & Ge, S. (2013). Finite element analysis of fretting fatigue behavior of steel wires and crack initiation characteristics. *Engineering Failure Analysis*, *28*, 47-62.

[5] Zeng, D., Zhang, Y., Lu, L., Zou, L., & Zhu, S. (2019). Fretting wear and fatigue in press-fitted railway axle: a simulation study of the influence of stress relief groove. *International Journal of Fatigue*, *118*, 225-236.

[6] Abazadeh, B., Chakherlou, T. N., & Alderliesten, R. C. (2013). Effect of interference fitting and/or bolt clamping on the fatigue behavior of Al alloy 2024-T3 double shear lap joints in different cyclic load ranges. *International Journal of Mechanical Sciences*, *72*, 2-12.

[7] Rajasekaran, R., & Nowell, D. (2006). Fretting fatigue in dovetail blade roots: Experiment and analysis. *Tribology international*, *39*(10), 1277-1285.

[8] Antoni, N. (2014). A study of contact non-linearities in pin-loaded lugs: Separation, clearance and frictional slipping effects. *International journal of non-linear mechanics*, *58*, 258-282.

[9] Erena, D., Vázquez, J., Navarro, C., & Talemi, R. (2020). Numerical study on the influence of artificial internal stress relief groove on fretting fatigue in a shrink-fitted assembly. *Tribology International*, *151*, 106443.

[10] Nesládek, M., Španiel, M., Jurenka, J., Růžička, J., & Kuželka, J. (2012). Fretting fatigue–Experimental and numerical approaches. *International Journal of Fatigue*, *44*, 61-73.

[11] Tomlinson, G. A., Thorpe, P. L., & Gough, H. J. (1939). An investigation of the fretting corrosion of closely fitting surfaces. *Proceedings of the Institution of Mechanical Engineers*, *141*(1), 223-249.

[12] Dobromirski, J. (1992). Variables of fretting process: are there 50 of them?. *ASTM Special Technical Publication*, *1159*, 60-60.

[13] Nishioka, K., & Kenji, H. (1972). Fundamental investigations of fretting fatigue: Part 6, effects of contact pressure and hardness of materials. *Bulletin of JSME*, *15*(80), 135-144.

[14] Mugadu, A., Hills, D. A., & Nowell, D. (2002). Modifications to a fretting-fatigue testing apparatus based upon an analysis of contact stresses at complete and nearly complete contacts. *Wear*, *252*(5-6), 475-483.

[15] Poovakaud, V. V., Jiménez-Peña, C., Talemi, R., Coppieters, S., & Debruyne, D. (2020). Assessment of fretting fatigue in high strength steel bolted connections with simplified Fe modelling techniques. *Tribology International*, *143*, 106083.

[16] Ruiz, C., Boddington, P. H. B., & Chen, K. C. (1984). An investigation of fatigue and fretting in a dovetail joint. *Experimental mechanics*, *24*(3), 208-217.

[17] Bickley, W. G. (1928). X. The distribution of stress round a circular hole in a plate. *Philosophical Transactions of the Royal Society of London. Series A, Containing Papers of a Mathematical or Physical Character*, *227*(647-658), 383-415.

[18] Chang, F. K., Scott, R. A., & Springer, G. S. (1982). Strength of mechanically fastened composite joints. *Journal of Composite materials*, *16*(6), 470-494.

[19] ABAQUS (2014) `ABAQUS Documentation', Dassault Systèmes, Providence, RI, USA.

[20] Blau, P. J. (2008). *Friction science and technology: from concepts to applications*. CRC press.

[21] Iwabuchi, A. (1991). The role of oxide particles in the fretting wear of mild steel. *Wear*, *151*(2), 301-311.

[22] Ciavarella, M., & Demelio, G. (2001). A review of analytical aspects of fretting fatigue, with extension to damage parameters, and application to dovetail joints. *International Journal of Solids and Structures*, *38*(10-13), 1791-1811.

[23] Fatemi, A., & Socie, D. F. (1988). A critical plane approach to multiaxial fatigue damage including out-of-phase loading. *Fatigue & Fracture of Engineering Materials & Structures*, *11*(3), 149-165.

[24] Fatemi, A., & Shamsaei, N. (2011). Multiaxial fatigue: An overview and some approximation models for life estimation. *International Journal of Fatigue*, *33*(8), 948-958.

[25] Navarro, C., Muñoz, S., & Dominguez, J. (2008). On the use of multiaxial fatigue criteria for fretting fatigue life assessment. *International Journal of fatigue*, *30*(1), 32-44.

[26] Jiménez-Peña, C., Talemi, R. H., Rossi, B., & Debruyne, D. (2017). Investigations on the fretting fatigue failure mechanism of bolted joints in high strength steel subjected to different levels of pre-tension. *Tribology International*, *108*, 128-140.

[27] Nowell, D., Dini, D., & Hills, D. A. (2006). Recent developments in the understanding of fretting fatigue. *Engineering fracture mechanics*, *73*(2), 207-222.

# APPENDICES

## A. Distribution of contact pressure and shear stresses at the lug mating surface

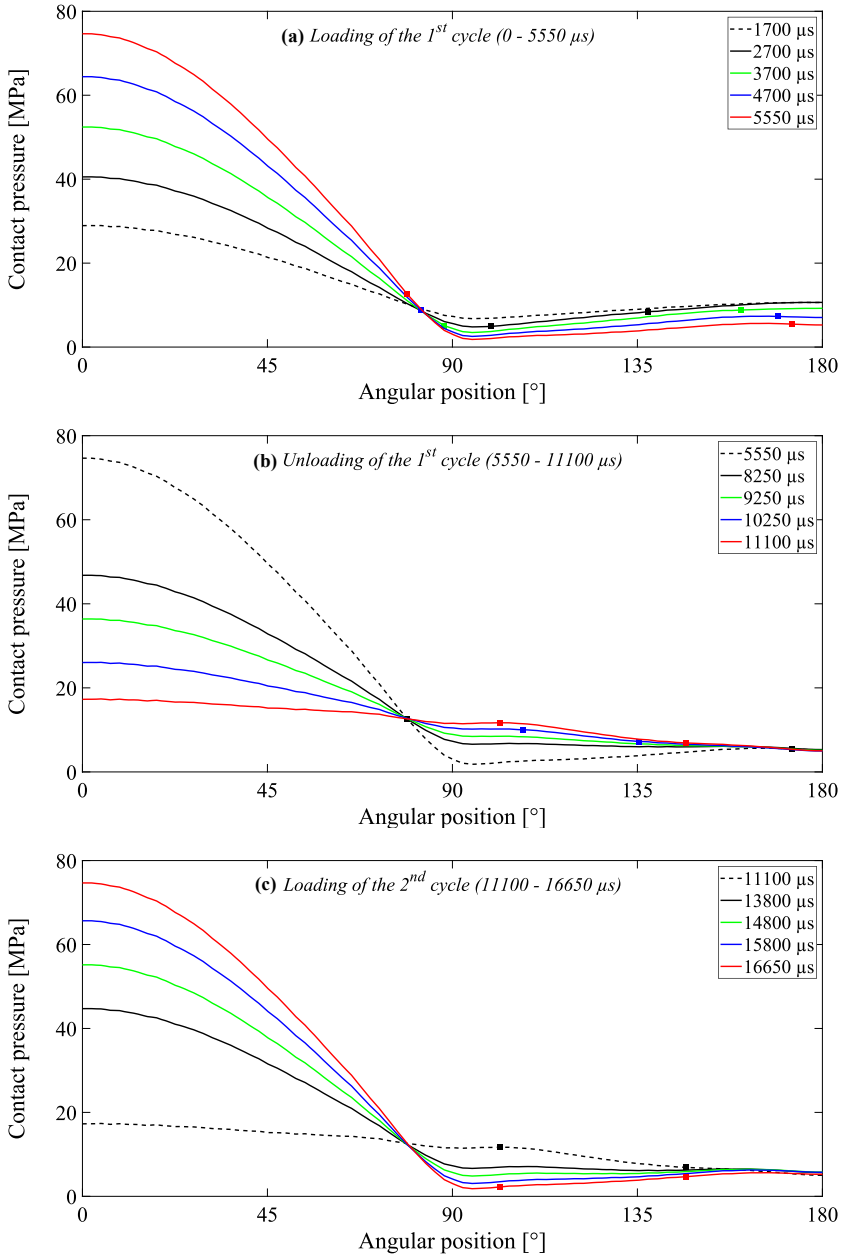


Figure A.7.1. Normal stress distributions along a circular path taken at the mid-thickness of the lug mating surface of the Al-Al lug bush member with $\mu$ = 0.8.

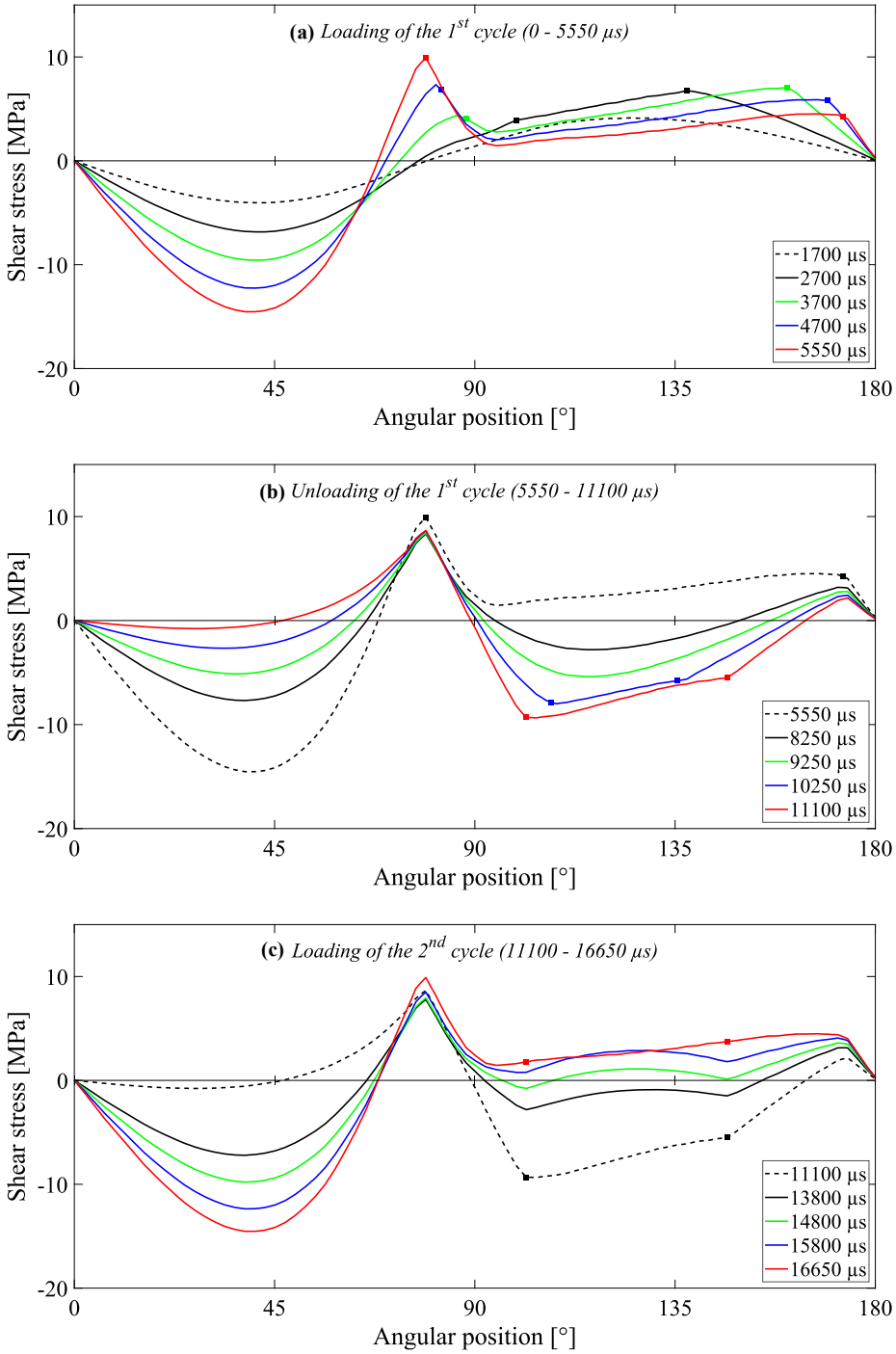


Figure A.7.2. Shear stress distributions along a circular path taken at the mid-thickness of the lug mating surface of the Al-Al lug bush member with $\mu$ = 0.8.

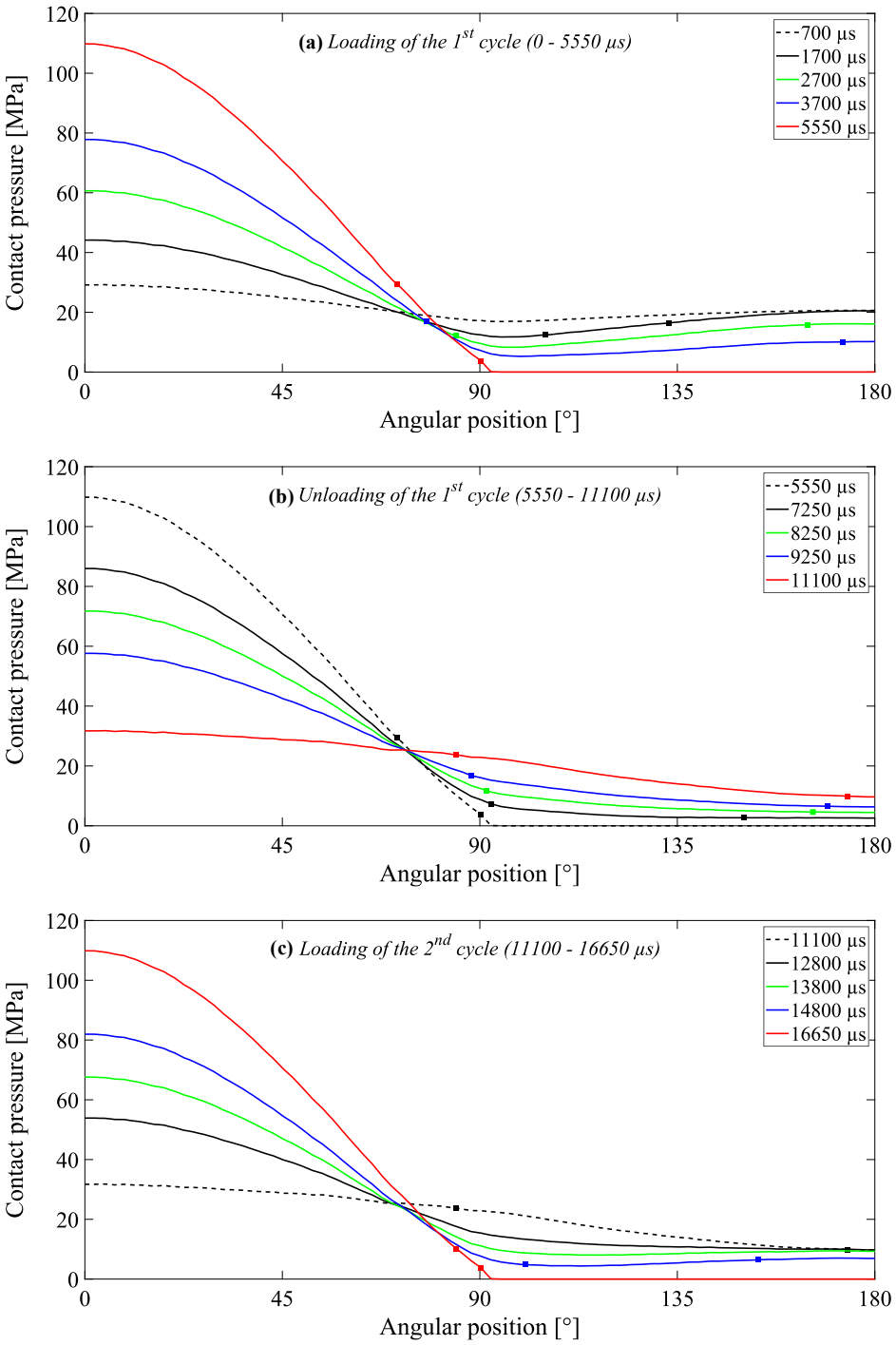


Figure A.7.3. Normal stress distributions along a circular path taken at the mid-thickness of the lug mating surface of the Al-steel lug bush member with $\mu = 0.6$.

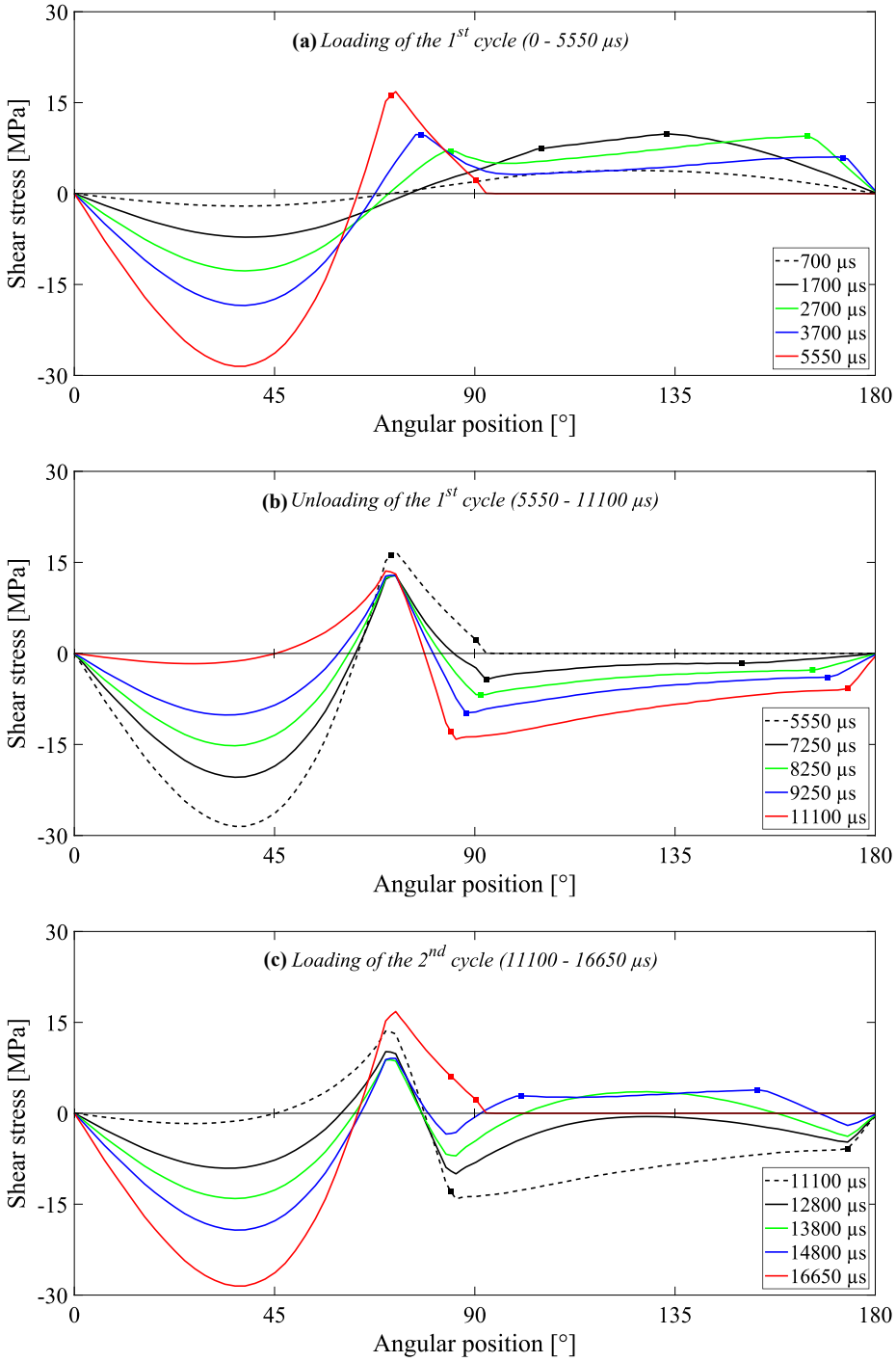


Figure A.7.4. Shear stress distributions along a circular path taken at the mid-thickness of the lug mating surface of the Al-steel lug bush member with $\mu$ = 0.6.

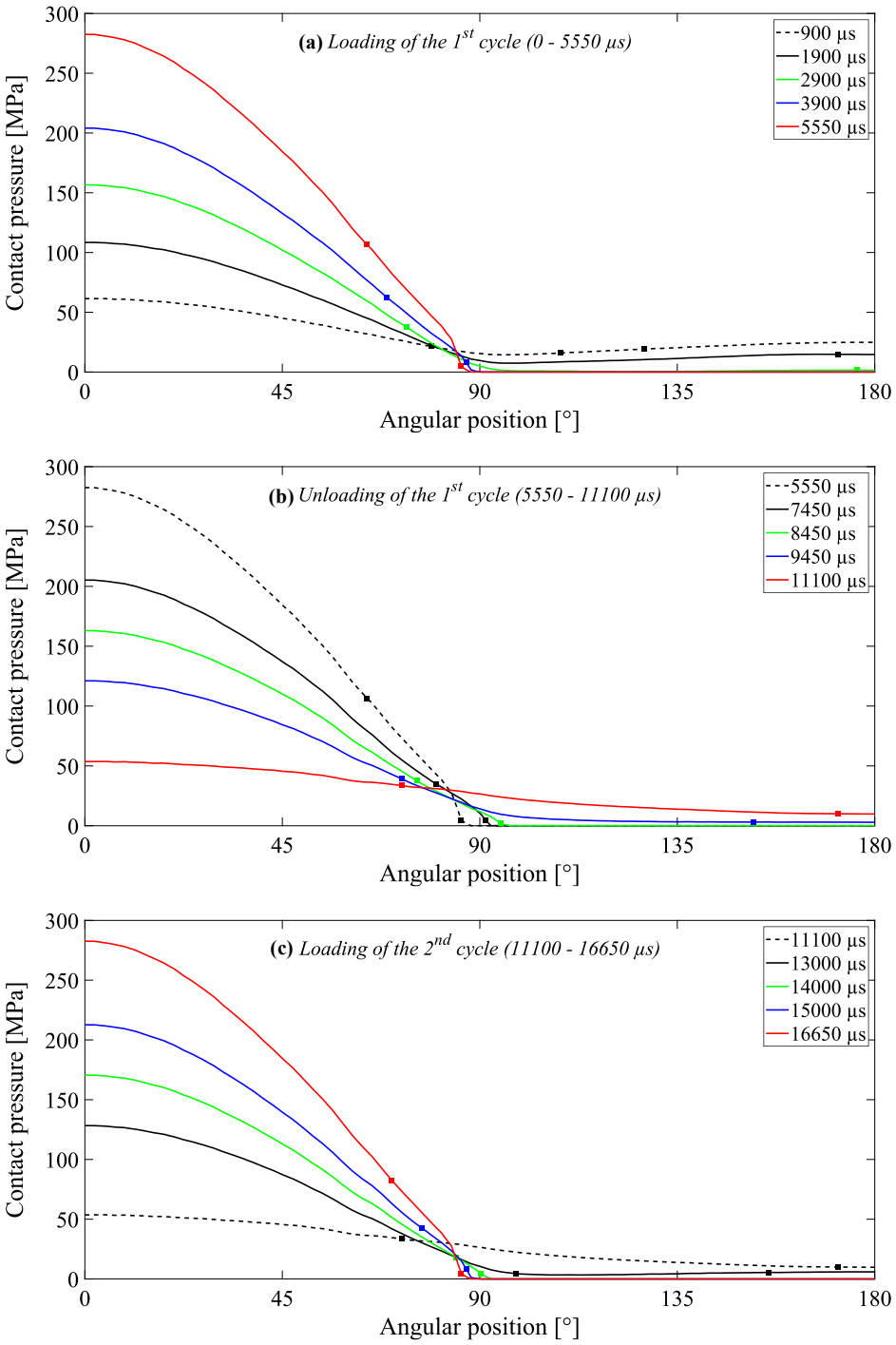


Figure A.7.5. Normal stress distributions along a circular path taken at the mid-thickness of the lug mating surface of the Ti-steel lug bush member with $\mu = 0.6$.

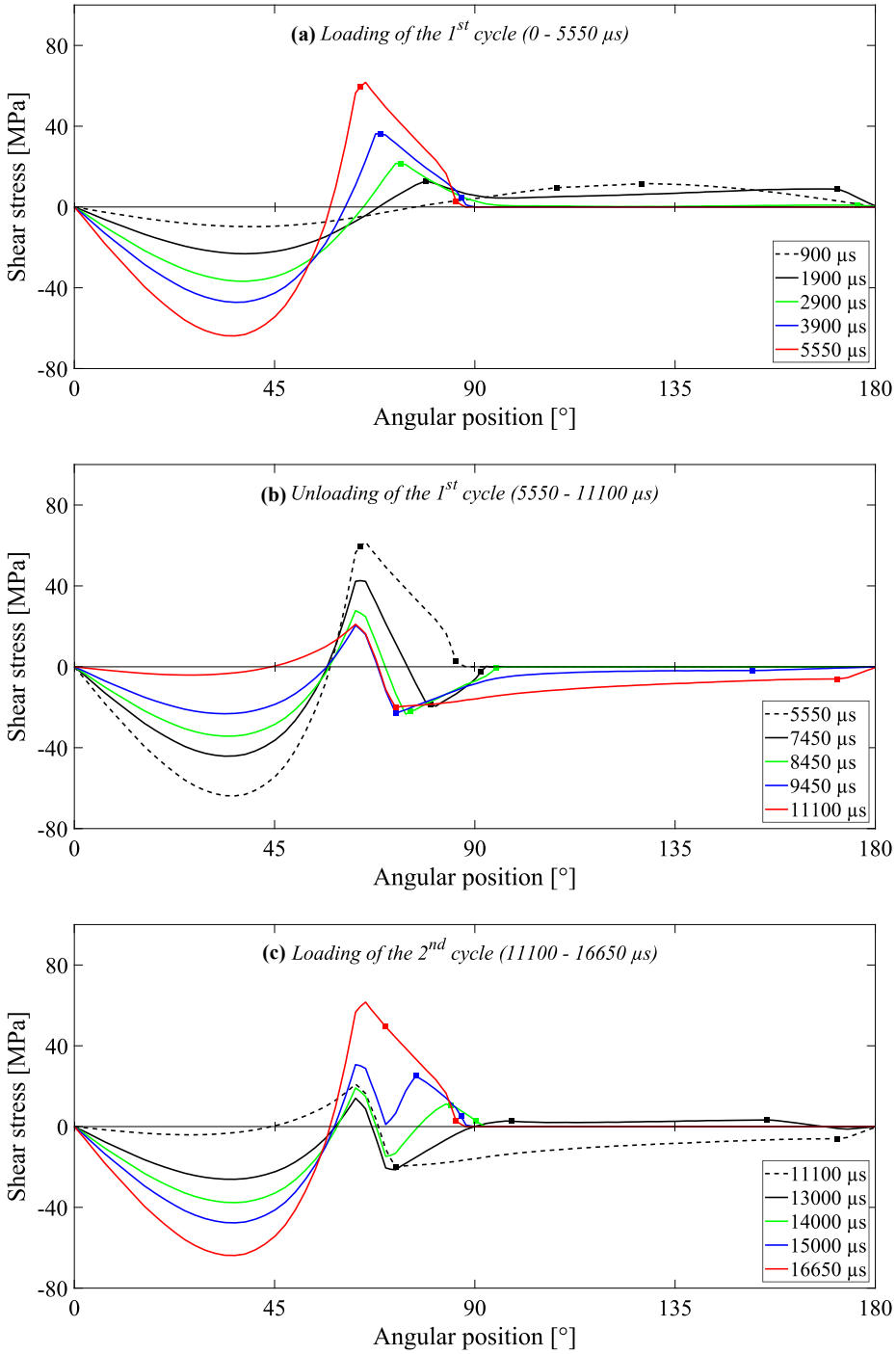


Figure A.7.6. Shear stress distributions along a circular path taken at the mid-thickness of the lug mating surface of the Ti-steel lug bush member with $\mu$ = 0.6.